

# Microstructure and micromechanical properties of magnesium phosphate cement

Guosheng Zhang<sup>a</sup>, Qiang Wang<sup>a\*</sup>, Yue Li<sup>b</sup>, Mingzhong Zhang<sup>c</sup>

<sup>a</sup> Department of Civil Engineering, Tsinghua University, Beijing 100084, China

<sup>b</sup> Key Laboratory of Urban Security and Disaster Engineering of Ministry of Education, Beijing Key Laboratory of Earthquake Engineering and Structural Retrofit, Beijing University of Technology, Beijing 100124, China

<sup>c</sup> Department of Civil, Environmental and Geomatic Engineering, University College London, London WC1E 6BT, UK

\*Corresponding author: w-qiang@tsinghua.edu.cn (Q. Wang)

**Abstract:** This paper presents a systematic study on the evolution of phase composition, microstructure and micromechanical properties of magnesium phosphate cement (MPC) and their relations to macroscopic mechanical properties. The results indicate that the microstructure of MPC is mainly composed of a crystal region of potassium magnesium phosphate hexahydrate (MKP) and a hybrid region of magnesium oxide and amorphous hydration products. The elastic modulus and hardness of MKP crystals are 20.18 GPa and 1.15 GPa, respectively. Amorphous hydration products may consist of  $\text{MgKPO}_4$  and  $\text{Mg}_3(\text{PO}_4)_2$ . The elastic modulus of amorphous  $\text{MgKPO}_4$  drops gradually from 51.4 GPa to 29.2 GPa with increasing curing age towards the elastic modulus of crystalline MKP, while the elastic moduli of amorphous  $\text{Mg}_3(\text{PO}_4)_2$  and unreacted MgO are approximately 160 GPa and 300 GPa, respectively. The macroscopic strength of MPC is mainly dependent on its pore structure rather than the micromechanical properties of hydration products.

**Keywords:** Magnesium phosphate cement; Microstructure; Micromechanics; Nuclear magnetic resonance; Nanoindentation

## 1. Introduction

Magnesium phosphate cement (MPC) is produced by an acid-base reaction between phosphate and magnesium oxide [1]. Compared with ordinary Portland cement, MPC has many advantages, such as high early strength, fast setting, good bonding performance and excellent biocompatibility. Thus, it has been widely used in repair and reinforcement [2, 3], solidification of heavy metals and radioactive elements [4, 5], biomedicine and other fields [6, 7].

The recent studies on MPC have mainly focused on the hydration process and phase composition. Cement paste suspensions are often used to explore the hydration mechanism of MPC with a molar

ratio of magnesium oxide to potassium dihydrogen phosphate (M/P) of 1 and a water-to-binder (w/b) ratio of 100. The hydration of MPC consists of multiple steps that can be evaluated based on the change in ions in the diluted suspension [8].  $\text{MgHPO}_4 \cdot 7\text{H}_2\text{O}$  first precipitated and then decomposed to form  $\text{Mg}_2\text{KH}(\text{PO}_4)_2 \cdot 15\text{H}_2\text{O}$ , followed by conversion to  $\text{KMgPO}_4 \cdot 6\text{H}_2\text{O}$  (MKP) and  $\text{Mg}_3(\text{PO}_4)_2 \cdot 22\text{H}_2\text{O}$ . It was reported that during the hydration of MPC, newberyite ( $\text{MgHPO}_4 \cdot 3\text{H}_2\text{O}$ ) was initially formed and gradually decomposed with increasing pH, which promoted the crystallization of MKP [9]. The pH and ion species in solution have a significant influence on the hydration of MPC. MKP is the main hydration product of MPC, and the hydration of MPC can be described as [10-12]:



The above conclusions about hydration were based on the suspension of MPC, which had a lower molar ratio of M/P and a higher w/b ratio. However, the MPC system used in practice often required a higher molar ratio of M/P (4-8) and a lower w/b ratio (0.1-0.2), which had excellent performance in this mix ratio range [13, 14]. At this time, it was difficult to prepare MPC suspensions at a high molar ratio of M/P and a low w/b ratio. Therefore, the above conclusions about hydration are not necessarily suitable for MPC systems with lower w/b ratios.

The hydration products of MPC with a low water-to-cement (w/c) ratio were mainly revealed by studying the solid phase. The crystalline hydration product of MPC is MKP, but there are many other amorphous hydration products present. For example, when the M/P ratio was 4 and the w/b ratio was 0.14, the mass content of the MPC amorphous phase exceeded 60% at 28 d [15]. According to  $^{31}\text{P}$  NMR analysis, with an M/P ratio of 4 and a w/b ratio of 0.25, many amorphous orthophosphates were observed in hydration products of MPC. It was speculated that amorphous  $\text{Mg}_3(\text{PO}_4)_2$  was formed while the specific composition of the amorphous phase was not further analysed [16]. Viani [17-20] confirmed through a series of experimental tests that many amorphous phases were also generated in MPC, even at a low M/P ratio. Unfortunately, it was still not feasible to determine the specific composition of these amorphous phases.

Microstructure plays a crucial role in the properties of MPC. As the main hydration product of MPC, the microstructure of MKP is closely related to the molar ratio of M/P. When M/P was small (less than 2), MKP grew into needle-like crystals with a large aspect ratio. With an increase in the M/P ratio, the morphology of MKP gradually exhibited a prismatic shape [21]. When the molar ratio

of M/P was in the range of 4~6, MPC contained more crystal MKP and had a dense microstructure and superior mechanical properties [22]. Although the microstructure of MKP was explored, the distribution of crystalline and amorphous hydration products as well as unreacted products in the microstructure is still unclear.

Nanoindentation is usually adopted to measure the micromechanical properties of various phases in cement-based materials. For instance, Ulm et al. [23-26] introduced the nanoindentation method for cement-based materials and developed a coupling analysis method to investigate the micromechanics-chemistry-structure relationships based on nanoindentation tests [27-30]. Some studies have also attempted to apply nanoindentation to MPC and found that the average elastic modulus of unreacted magnesium oxide was approximately 300 GPa, and the average elastic modulus of hydrated products was about 35 GPa [31-34]. In literature, the average elastic moduli of hydration products were obtained through nanoindentation statistics, without an in-depth analysis of the elastic moduli of crystalline and amorphous hydration products as well as their contributions to the overall macroscopic mechanical properties of MPC, and the evolution of micromechanical properties of hydration products with curing age was not extensively explored. Moreover, the elastic modulus of unreacted magnesium oxide was found to be approximately 100 GPa [34] and 300 GPa [32, 33], respectively, indicating a large discrepancy.

At present, the phase composition of MPC is still unclear, especially the composition and content of the amorphous phase. What is the distribution of crystal and amorphous hydration products and unreacted substances in the microstructure of MPC? There is still a lack of systematic understanding of the micromechanical properties of each phase in MPC and the relationships between the micromechanical properties and the macroscopic mechanical properties.

To fill in the knowledge gaps, in this study, the micromechanical properties of crystalline and amorphous phase hydration products were systematically investigated using nanoindentation for the first time, as well as the phase composition, microstructure and micromechanics of MPC. The phase composition of MPC was measured by X-ray diffraction (XRD), thermogravimetry (TG), Fourier transform infrared spectroscopy (FTIR), and nuclear magnetic resonance (NMR) spectroscopy. The microstructure and pore structure of MPC were characterised using backscattering electron microscopy (BSEM) and mercury intrusion porosimetry (MIP). The micromechanical properties (elastic modulus and hardness) of the phase in MPC were measured by nanoindentation. Based on

the obtained experimental data, the development of micromechanical properties of each phase in MPC with curing age was explored and the relationships between micromechanical properties of each phase in MPC and the macroscopic properties of MPC were estimated and discussed in depth.

## 2. Experimental program

### 2.1 Materials and mix proportion

In this study, the raw materials used to produce MPC paste include calcined magnesium oxide (calcined at 1600 °C), potassium dihydrogen phosphate, deionized water and borax (sodium tetraborate). Potassium dihydrogen phosphate and borax were analytically pure and purchased from Shanghai Titan Technology Co., Ltd. The chemical composition and physical properties of calcined magnesium oxide are presented in Table 1. The density of calcined magnesium oxide is 3.46 g/cm<sup>3</sup>, which mainly contains 88.2% MgO, 5.6% SiO<sub>2</sub>, and 3.5% CaO. The particle size distribution of magnesium oxide is shown in Fig. 1, indicating that the particle size of magnesium oxide is mainly distributed in the range of 0.2-200 μm. d(0.5) and d(0.9) are 32.8 μm and 94.6 μm, respectively.

As per the relevant literature [35-37] and our previous studies [38, 39], the optimal mix proportion of MPC is determined, as given in Table 2. The molar ratio M/P of magnesium oxide to potassium dihydrogen phosphate is 4.5. The w/b ratio is 0.14, and the borax content is 5% of magnesium oxide.

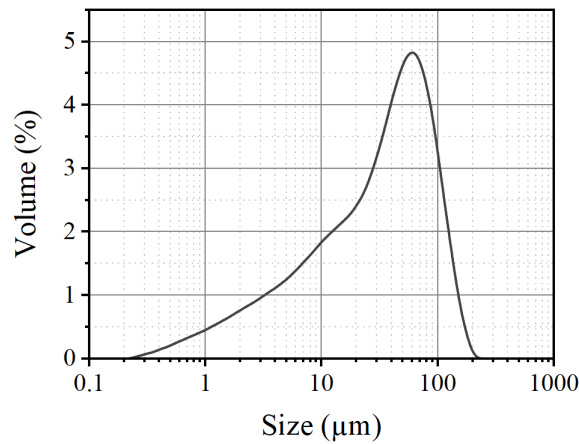


Fig. 1. Particle size distribution of calcined magnesium oxide.

Table 1 Chemical composition and physical properties of calcined magnesium oxide.

Sample	MgO (%)	SiO <sub>2</sub> (%)	CaO (%)	Fe <sub>2</sub> O <sub>3</sub> (%)	Al <sub>2</sub> O <sub>3</sub> (%)	Density (g/cm <sup>3</sup> )	Bulk density (g/cm <sup>3</sup> )	Specific surface area (cm <sup>2</sup> /g)
MgO	88.2	5.6	3.5	1.2	0.7	3.46	1.67	805.9

Table 2 Mix proportion of MPC.

MgO (g)	KH <sub>2</sub> PO <sub>4</sub> (g)	Water (g)	Borax (g)
1140	860	280	57

## 2.2 Specimen preparation

The prepared MPC paste was poured into a plastic mould of 160×160×40 mm and covered with plastic film for curing (23 °C). The mould was removed one day later, and the sample was cured in an environment with a relative humidity of 50% and a temperature of 23 °C for test ages of 1, 3, 7 and 28 d. At each test age, a small cylindrical specimen with a diameter of 5 mm and a height of 2 mm was cut from the specimen via wire cutting. The specimen was stored in isopropanol solution for 2 d to stop MPC from continuing hydration and then dried in a drying oven at 40 °C.

The samples were further prepared to meet the requirements for different tests. MPC was ground for XRD, TG, FTIR and NMR tests. Small cylindrical specimens were embedded in epoxy resin and polished to meet the surface roughness requirement for nanoindentation test. The equipment and consumables from Struers were used for polishing. Initially, the samples were embedded in epoxy resin from an EpoFix Kit and vacuum impregnated in a CitoVac instrument. The epoxy resin of the EpoFix Kit had a low viscosity, and the mass ratio of resin to hardener was 25:3. The samples were then polished with a LaboPol-30 polishing machine. MD-Piano 500, MD-Piano 1200, MD-Largo, MD-Dac and MD-Nap grinding discs and polishing cloths were used in turn. Additionally, 9 µm, 3 µm, and 1 µm diamond suspensions were used for polishing. Note that after each polishing process, the samples were cleaned via ultrasonic waves in absolute ethanol to remove the residual diamond suspension from the sample surface.

## 2.3 Testing methods

### 2.3.1 Isothermal conduction calorimetry (ICC)

A TAM-Air isothermal calorimeter was used to measure the heat release during the hydration process of MPC. According to the mix ratio in [Table 2](#), potassium dihydrogen phosphate and magnesium oxide were mixed for 2 min, followed by the addition of deionized water according to the proportion. The paste was stirred internally for 2 min. The test ambient temperature was 20°C.

### 2.3.2 Phase composition

XRD, TG, FTIR and NMR tests were performed to investigate the phase composition of MPC at different ages (1, 3, 7 and 28 d). For XRD analysis, a Bruker D8 Advance instrument was used in continuous scanning mode. The scanning angle ranged from 10° to 80° (2θ), and the scanning speed was 2°/min. A NETZSCH STA 2500 instrument was used for TG test. The sample mass was 50 mg. The temperature range was 25 °C-1000 °C, and the heating rate was 10 °C/min. The test environment

was nitrogen, and the crucible material was alumina oxide.

As a supplement to XRD test, FTIR spectroscopy was adopted to identify the characteristics of crystalline and amorphous phases in MPC. FTIR spectra were measured with a Nicolet iS50 instrument, and the wavenumber ranged from 400 cm<sup>-1</sup> to 4000 cm<sup>-1</sup>.

<sup>31</sup>P and <sup>31</sup>P-<sup>1</sup>H cross-polarization (CP) NMR spectra were measured using a JNM-ECZ600R (14.1 T) solid-state nuclear magnetic resonance spectrometer. The testing parameters including rotor diameter, Larmor frequency, pulse duration, relaxation delay and number of scans were set as 3.2 mm, 242.8 MHz, 5 μs, 5 s, 12 kHz and 128, respectively.

### 2.3.3 Microstructure characterisation

The microstructure and pore structure of MPC were characterised using BSEM and MIP. BSEM test was carried out using a TESCAN MIRA LMS instrument with a resolution of 0.9 nm, an acceleration voltage of 15 keV, and a probe beam current of 100 pA. Gold was sprayed on the sample to obtain better conductivity. As an important feature of MPC, pore structure is closely related to mechanical properties of MPC. A MicroActive AutoPore V 9600 instrument was used for MIP testing with a pressure range of 0.1-61000 psia. The contact angle of mercury was 130°, and the surface tension was 0.485 N/m.

### 2.3.4 Mechanical properties

The micromechanical properties (elastic modulus and hardness) of different phases in MPC paste were characterised using nanoindentation. A G200 nanoindentation instrument and a diamond Berkovich indenter (triangular pyramid, with an angle of 65.3° between the edge and the centreline) were used in this study. Based on the indentation load–displacement curve, the elastic modulus ( $E$ ) and hardness ( $H$ ) can be calculated as follows:

$$E = (1 - \nu^2) \cdot \left[ \frac{2\beta}{S} \sqrt{\frac{A}{\pi}} - \frac{1-\nu_i^2}{E_i} \right]^{-1} \quad (2)$$

$$H = \frac{p}{A} \quad (3)$$

where  $\nu$  is the Poisson's ratio of the tested material,  $\beta$  is the correction factor ( $\beta = 1.034$ ),  $S$  is the contact stiffness,  $A$  is the contact area,  $\nu_i$  and  $E_i$  are the Poisson's ratio and elastic modulus of the diamond indenter ( $\nu_i = 0.07$ ,  $E_i = 1141$  GPa), and  $p$  is the indenter load.

In the nanoindentation test, the maximum indentation load was 2 mN, while the loading and

unloading rate was 66.67  $\mu\text{N/s}$ . The loading time and unloading time were both 30 s, and the re-loading time was 10 s. Two modes of typical nanoindentation and grid nanoindentation were adopted. Typical nanoindentation test was performed on typical unreacted products and reaction products in MPC to obtain the basic mechanical properties of them. Grid nanoindentation was used to select a region of interest in MPC and test the indentation matrix with a spacing of 10  $\mu\text{m}$  for subsequent statistical analysis. For example, the  $11 \times 11$  indentation matrix was measured in a region of interest of MPC at each age, and the micromechanical property distribution of each phase in the region of  $100 \times 100 \mu\text{m}$  was obtained.

At 1, 3, 7 and 28 d, the compressive strength and flexural strength of the three specimens were tested by a universal testing machine, and the average value and standard deviation were determined. The loading rates of the flexural and compressive tests were 0.6 kN/s and 2.4 kN/s, respectively.

### 3. Results and discussion

#### 3.1 Hydration heat evolution

Fig. 2 displays the hydration heat release rate of MPC. The exothermic rate curve goes up rapidly and then drops rapidly, approaching zero. The first drop in exothermic rate curve can be ascribed to the heat absorption due to the dissolution of potassium dihydrogen phosphate in water. After that, the exothermic rate curve rises sharply and reaches the peak value of approximately 150 mW/g in about 10 min, reflecting the intense hydration reaction of MPC. Then, the heat release rate curve drops rapidly, and the heat release rate at 0.5 h reduces to 1/10 of the peak value, followed by a slow drop in heat release rate. The heat release rate at 3 h reduces to 3 mW/g. At that moment, the heat release is smaller than that at 10 min. As the hydration of MPC is an acid-base reaction, it reacts rapidly in a short time with a large amount of heat release, followed by a short decrease in heat [14].

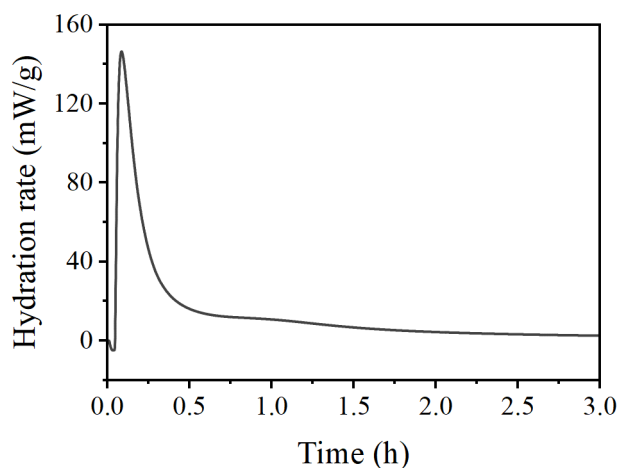


Fig. 2. Evolution of hydration heat rate of MPC.

### 3.2 Phase composition

#### 3.2.1 XRD analysis

MPC samples with different curing ages were doped with 20% CaF<sub>2</sub> for XRD test, the results of which are presented in Fig. 3. The hydration product (MKP) and unreacted MgO are the main phases in MPC while the reactant potassium dihydrogen phosphate is not found. XRD data were semi-quantitatively analysed using TOPAS software. The results are given in Table 3, where the phase composition is percentage by mass. With increasing curing age, the amount of hydration product (MKP crystals) increases greatly, from 13.4% to 23.4%. The content of unreacted MgO drops gradually from 37.1% to 33.5%. A large number of amorphous phases in MPC (exceeding 40% at all ages) are formed as the w/c ratio was low and the content of water is not enough for crystallization of all hydration products. However, the amorphous phase content reduces from 47.4% to 41.2% with increasing curing age, while the content of hydration product (MKP crystal) rises, which can be ascribed to the continuous hydration of reactant MgO particles and the transformation of amorphous phase. Meanwhile, it can also be observed that MPC contains about 2% of Monticellite at different curing ages, due to the presence of Monticellite in the raw material of magnesium oxide.

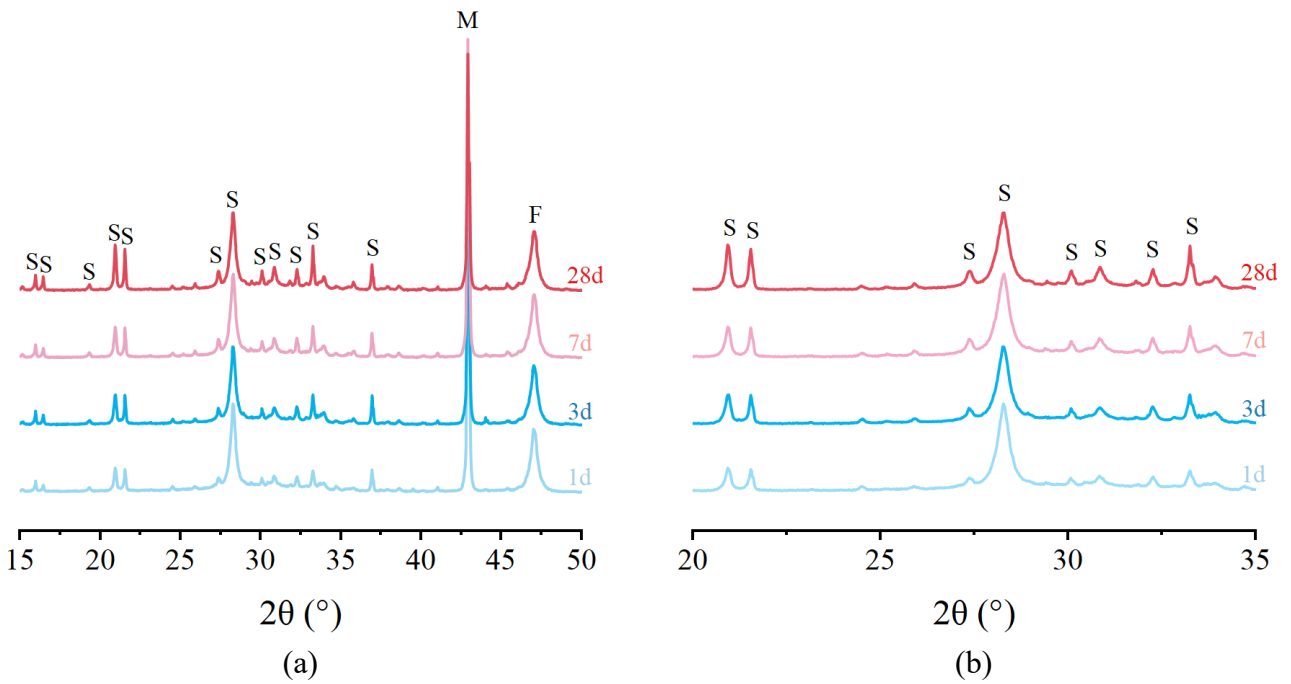


Fig. 3. XRD curves of MPC at different curing ages (S = MgKPO<sub>4</sub>·6H<sub>2</sub>O, M = MgO, F = CaF<sub>2</sub>).

Table 3 Phase mass content of MPC determined by XRD data.

Sample	Struvite-K (%)	Periclase (%)	Amorphous (%)	Monticellite CaMgSiO <sub>4</sub> (%)
--------	----------------	---------------	---------------	---------------------------------------

MPC-1d	13.4	37.1	47.4	1.7
MPC-3d	18.4	34.8	44.5	2.1
MPC-7d	17.5	36.2	44.6	1.5
MPC-28d	23.4	33.5	41.2	1.6

### 3.2.2 Thermogravimetric analysis

Fig. 4 and Table 4 illustrate the thermogravimetric test results of MPC at different curing ages. The relative quality refers to the ratio of the mass of a substance after weightlessness during heating to the quality before heating. With increasing curing age, the relative quality gradually decreases from 86.9% at 1 d to 82.0% at 28 d, while the mass loss goes up from 13.1% at 1 d to 18.0% at 28 d. Assuming that the hydration products of the thermogravimetric decomposition are all crystalline MKP, the decomposition equation is given as Eq. (4). The mass of MKP crystal is 2.46 times the weight loss mass; the theoretical calculation of the MKP crystal content at 1 d and 28 d is 32.2% and 44.2%, respectively. However, as per the XRD analysis, the content of MKP crystals at 1 d and 28 d is 13.4% and 23.4%, respectively, much lower than that obtained from theoretical calculation. Thus, the hydration products of MPC also contain amorphous hydration products in addition to MKP crystals, and the water content of the amorphous phase is less than that of MKP crystal.

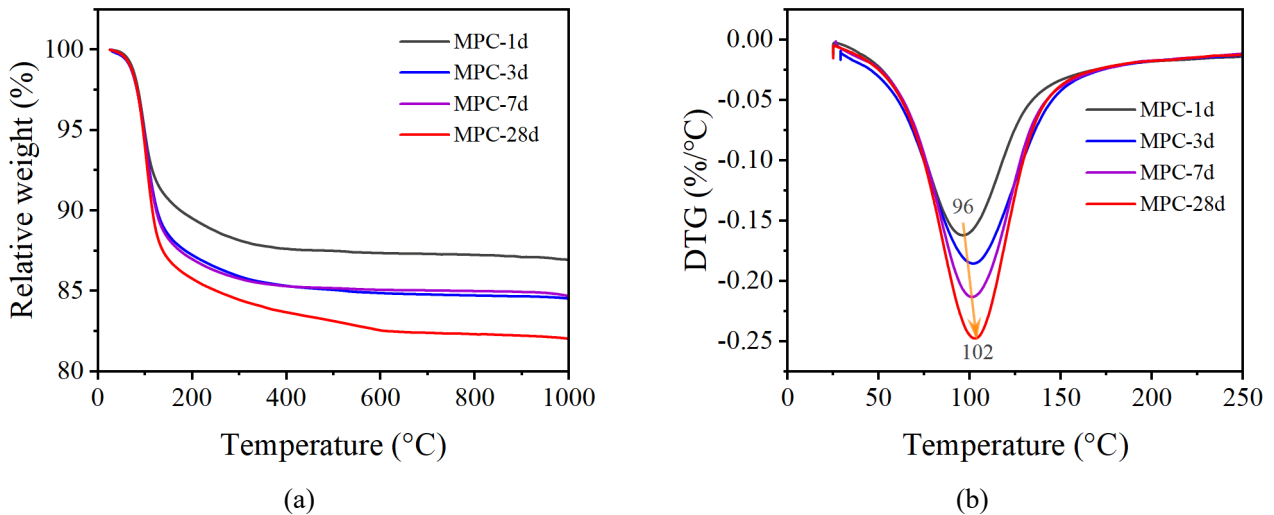


Fig. 4. TG and DTG curves of MPC at different curing ages.

The hydration products are mainly decomposed in the range of 50-160 °C. The DTG curve in this range is amplified and analysed, as shown in Fig. 4(b). The peak value of DTG changes from -0.16%/°C at 1 d to -0.25%/°C at 28 d, and the position of the DTG peak shifts from 96 °C at 1 d to 102 °C at 28 d. This is because more hydration products are formed with the increase of curing age, resulting in a higher peak value of DTG. Meanwhile, more heat is required to make the hydration products lose

crystal water, and thus the position of DTG peak also moves slightly to the right.

Table 4 TG calculation results of MPC at different curing ages.

Sample	Relative weight (%)	Mass loss (%)
MPC-1d	86.9	13.1
MPC-3d	84.5	15.5
MPC-7d	84.7	15.3
MPC-28d	82.0	18.0

### 3.2.3 FTIR spectroscopy

Fig. 5 shows the evolution of MPC functional groups with time, characterised using IR spectra. MPC exhibits a wide and strong vibrational band near  $2946\text{ cm}^{-1}$ , which can be attributed to the H-O-H stretching vibrations of water in hydration products. The vibration band at approximately  $573\text{ cm}^{-1}$  can be assigned to the vibration of  $\text{PO}_4^{3-}$ . A more detailed analysis of the spectrum in the range of  $800\text{-}1200\text{ cm}^{-1}$  is presented in Fig. 5(b). The  $\text{PO}_4$  unit symmetric stretching vibration of crystal MKP is located at  $1023.5\text{ cm}^{-1}$  [40]. MPC generates a strong vibration band near  $1015\text{ cm}^{-1}$ , which corresponds to the mixing vibration band of crystalline MKP and amorphous hydration products. With the increase of curing age, the position of the vibration band peak shifts from  $1010\text{ cm}^{-1}$  to  $1016\text{ cm}^{-1}$ , implying that the content of crystalline MKP in hydration products increases. The vibration band at  $1081\text{ cm}^{-1}$  can be ascribed to the amorphous phase containing the  $\text{PO}_4$  unit [19, 41]. The vibration band at  $1081\text{ cm}^{-1}$  of the amorphous phase becomes weaker with the prolongation of curing age, while the vibration band at  $1016\text{ cm}^{-1}$  becomes stronger. This indicates that the content of amorphous phase reduces while the content of MKP rises in hydration products of MPC, which is consistent with the XRD results.

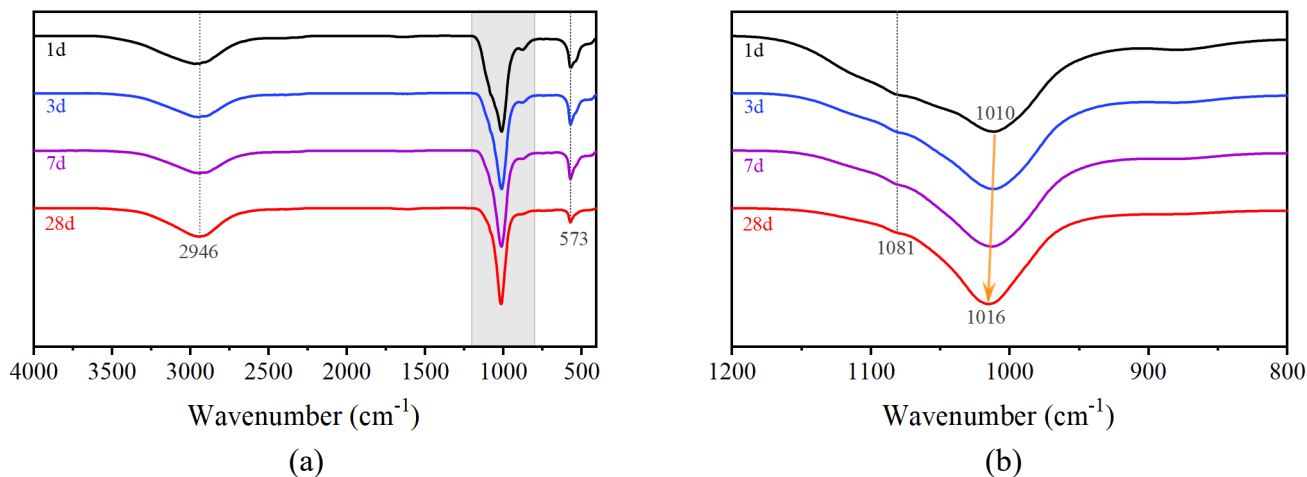


Fig. 5. Infrared curves of MPC at different curing ages: (a) spectra in the range of  $450\text{-}4000\text{ cm}^{-1}$ ,

and (b) spectra in the range of 800-1200  $\text{cm}^{-1}$ .

### 3.2.4 NMR spectroscopy

$^{31}\text{P}$  and  $^1\text{H}$ - $^{31}\text{P}$  CP NMR tests were performed on MPC at 1, 3, 7 and 28 d, the results of which are presented in Fig. 6. The  $^{31}\text{P}$  NMR data containing magnesium and potassium obtained from literature are summarised in Table 5. In the  $^{31}\text{P}$  spectrum, the shift of  $\text{KH}_2\text{PO}_4$  (KDP) is 4 ppm, which is consistent with those reported in literature, i.e., 4.1 ppm [42] and  $3.9 \pm 0.1$  ppm [43]. The  $^{31}\text{P}$  spectrum of MPC is a broad peak ranging from -12 ppm to 12 ppm, which reflects the characteristics of the NMR spectrum of amorphous phase. The shoulder peak at 6.4 ppm of the  $^{31}\text{P}$  spectrum corresponds to the chemical shift of MKP crystal, which agrees well with the reported shifts of  $6.4 \pm 0.1$  ppm [43] and 6.2 ppm [44, 45]. The shoulder peak at 6.4 ppm rises gradually with increasing curing age, suggesting that the content of MKP crystals in hydration products goes up with curing age. The chemical shift of  $\text{MgHPO}_4 \cdot 7\text{H}_2\text{O}$  is 1.7 ppm [43], while the chemical shift of  $\text{Mg}_3(\text{PO}_4)_2$  is 0.6 ppm [42] or 0.5 ppm [46] and that of amorphous  $\text{Mg}_3(\text{PO}_4)_2$  is 1.23-1.9 ppm [17] or 0.5 ppm [47]. In addition, the shift of amorphous  $\text{MgHPO}_4$  was found to occur at -2.4 ppm [47]; thus, the weak peak at -2 ppm in the  $^{31}\text{P}$  spectrum may correspond to amorphous  $\text{MgHPO}_4$ , which gradually rises with increasing curing age. Therefore, the broad peaks from -12 ppm to 12 ppm in the  $^{31}\text{P}$  spectrum may be composed of amorphous phases of  $\text{MgKPO}_4 \cdot \text{XH}_2\text{O}$ ,  $\text{MgHPO}_4 \cdot 7\text{H}_2\text{O}$ ,  $\text{Mg}_3(\text{PO}_4)_2$  and  $\text{MgHPO}_4$ .

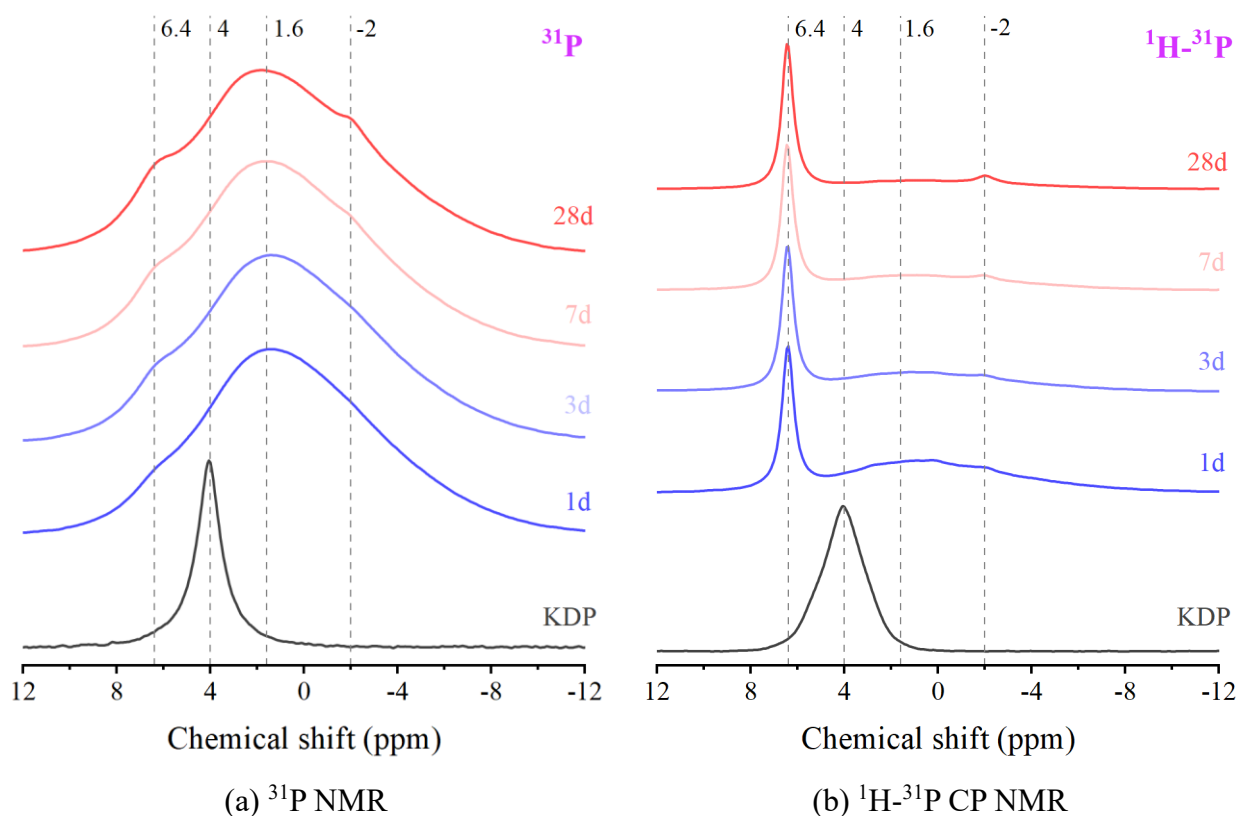


Fig. 6. NMR spectra of MPC at different curing ages: (a)  $^{31}\text{P}$  NMR, (b)  $^1\text{H}$ - $^{31}\text{P}$  CP NMR.

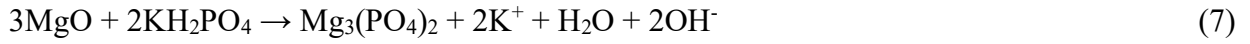
Table 5 Summary of  $^{31}\text{P}$  NMR data containing magnesium and potassium obtained from literature.

Mineral	$^{31}\text{P}$ ( $\delta$ , ppm)
$\text{MgNaPO}_4 \cdot 6\text{H}_2\text{O}$	wide peak centred on +8.6 [17]
Cattiite: $(\text{Mg}_3(\text{PO}_4)_2 \cdot 22\text{H}_2\text{O})$	+6.9±0.1 [43]
Struvite-K: $\text{MgKPO}_4 \cdot 6\text{H}_2\text{O}$	+6.9 [17], +6.7 [20], +6.4±0.1 [43], +6.2 [44, 45]
$\text{KH}_2\text{PO}_4$	+4.1 [42], +3.9±0.1 [43]
$\text{Mg}_2\text{KH}(\text{PO}_4)_2 \cdot 15\text{H}_2\text{O}$	2.6、3.1、3.4 and 3.7 [43]
Phosphorösslerite: $\text{MgHPO}_4 \cdot 7\text{H}_2\text{O}$	+1.7 [43],
Amorphous $\text{Mg}_3(\text{PO}_4)_2$	1.23-1.9 [17], +0.5[47]
$\text{Mg}_3(\text{PO}_4)_2$	+0.6 [42], +0.5 [46], -0.5 [47]
Amorphous $\text{MgHPO}_4$	-2.4 [47]
Newberyite: $\text{MgHPO}_4 \cdot 3\text{H}_2\text{O}$	-7.2 [46], -7.5±0.1 [43], -8 [47]
Q0(1Mg)	+4 [46]
Q0(2Mg)	-1 [46]
Q0(3Mg)	-7 [46]
$\text{KMgPO}_4$	*

\* No data currently available in open literature.

To further clarify the composition of  $^{31}\text{P}$  spectrum,  $^1\text{H}$ - $^{31}\text{P}$  NMR tests were performed, as illustrated in Fig. 6(b). In the  $^1\text{H}$ - $^{31}\text{P}$  NMR spectra, there are evident peaks near 6.4 ppm, 4 ppm and -2 ppm, corresponding to MKP crystal,  $\text{KH}_2\text{PO}_4$  and  $\text{MgHPO}_4$ , respectively. In addition, the broad peaks in the  $^{31}\text{P}$  spectra do not appear in the  $^1\text{H}$ - $^{31}\text{P}$  spectra, and there is only a sharp peak at 6.4 ppm in the  $^1\text{H}$ - $^{31}\text{P}$  spectra. This indicates that there is almost no interaction between H and P in the amorphous phases of MPC and the composition of the amorphous phases contains very little  $\text{H}_2\text{O}$ . As the possible amorphous phase of  $\text{MgHPO}_4 \cdot 7\text{H}_2\text{O}$  inferred from  $^{31}\text{P}$  spectra is disregarded,  $\text{Mg}_3(\text{PO}_4)_2$  is most likely the possible amorphous phase, and the value of X in  $\text{MgKPO}_4 \cdot \text{XH}_2\text{O}$  is presumably 0;  $\text{MgKPO}_4 \cdot \text{XH}_2\text{O}$  is mainly water-free  $\text{MgKPO}_4$ . In the  $^1\text{H}$ - $^{31}\text{P}$  spectrum of MPC-1d, there is a low and wide peak in the range of -2 ppm to 4 ppm, which gradually drops with curing age and disappears at 28 d. This peak is possibly an amorphous phase containing water, which gradually transforms into other phases with the increase of curing age. For instance,  $\text{MgKPO}_4 \cdot \text{XH}_2\text{O}$  containing some water gradually changes into MKP crystals with curing age. Therefore, based on the analysis of  $^{31}\text{P}$  and  $^1\text{H}$ - $^{31}\text{P}$  spectra, the phase compositions of MPC are potentially MgO, MKP crystal,  $\text{MgKPO}_4$ ,  $\text{Mg}_3(\text{PO}_4)_2$  and  $\text{MgHPO}_4$ , and the hydration reaction of MPC can be described as follows [47]:





In the hydration process of MPC, when the water consumption is sufficient, hydration can be mainly expressed as Eq. (5). The MKP crystal is the main hydration product, similar to the findings for MPC with high w/b ratios [8-12]. When the w/b ratio of MPC is low and the water consumption is less than the stoichiometric fully-hydrated water according to Eq. (5), a large number of amorphous phases without water are formed in hydration products of MPC, apart from MKP [14, 16]. At this time, MPC may undergo the hydration, as described in Eqs. (6)-(8).

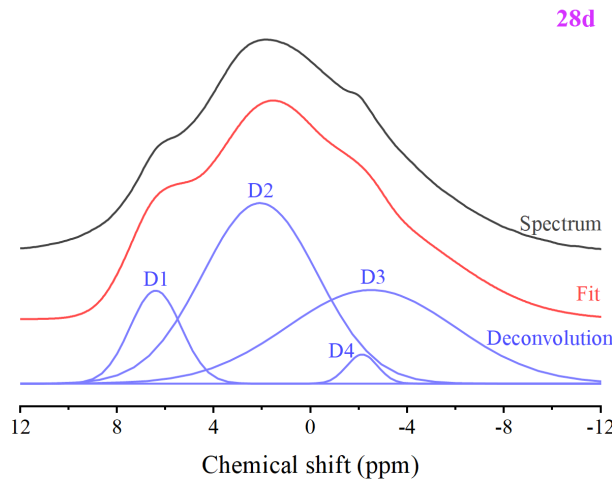


Fig. 7.  $^{31}\text{P}$  spectral deconvolution of MPC at 28 d.

Assuming that the  $^{31}\text{P}$  spectrum of MPC components conforms to a Gaussian distribution, the  $^{31}\text{P}$  spectrum of MPC-28d is deconvolved, as displayed in Fig. 7. Thus, the composition evolution of phosphorus-containing phase in the  $^{31}\text{P}$  spectrum can be further discussed. The black curve denotes the original  $^{31}\text{P}$  NMR experimental data, while the light blue curves are the deconvolution curves and the red curve is the fitting curve. According to the chemical shift distribution characteristics of the phases (Table 5), D1-D4 correspond to MKP crystal, amorphous  $\text{MgKPO}_4$ , amorphous  $\text{Mg}_3(\text{PO}_4)_2$  and amorphous  $\text{MgHPO}_4$ , respectively. As per the area proportion of the deconvolution curve, the content of phosphorus-containing phase can be calculated (Table 6). The content of MKP rises slightly with increasing curing age. The centre shift of amorphous  $\text{MgKPO}_4$  is approximately 2.1 ppm, and the content goes up from 44.40% at 1 d to 49.27% at 28 d. The chemical shift of amorphous  $\text{Mg}_3(\text{PO}_4)_2$  is approximately -2.20 ppm, while the content decreases gradually with time. The content of amorphous  $\text{MgHPO}_4$  is very low, less than 2%, and the chemical shift is approximately -2 ppm.

The change in the above phase content indicates that the phosphorus-containing phases undergo a certain transformation with curing age. For example, amorphous  $\text{Mg}_3(\text{PO}_4)_2$  could decompose and transform into  $\text{MgKPO}_4$  which then combines with some water to transform into MKP crystals.

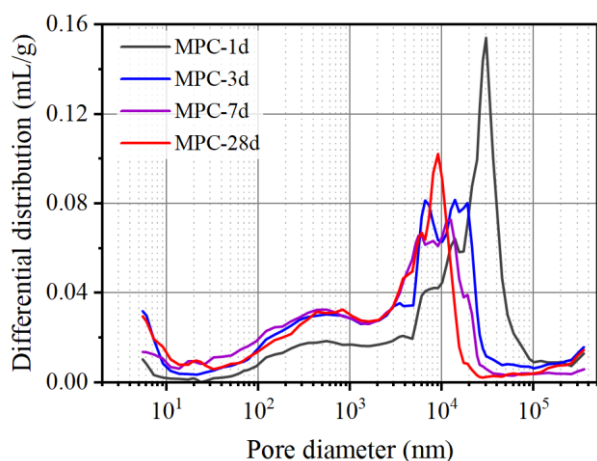
Table 6 Content of the phosphorus-containing phase calculated based on the area of the deconvolution curve of  $^{31}\text{P}$  spectrum.

Sample	MKP crystal		Amorphous $\text{MgKPO}_4$		Amorphous $\text{Mg}_3(\text{PO}_4)_2$		Amorphous $\text{MgHPO}_4$	
	Centre (ppm)	Percentage (%)	Centre (ppm)	Percentage (%)	Centre (ppm)	Percentage (%)	Centre (ppm)	Percentage (%)
MPC-1d	6.40	8.40	2.08	44.40	-2.10	46.04	-1.81	1.15
MPC-3d	6.35	9.43	2.04	46.56	-2.39	42.56	-1.89	1.45
MPC-7d	6.40	9.92	2.17	46.61	-2.20	41.96	-2.00	1.51
MPC-28d	6.40	11.33	2.09	49.27	-2.48	37.27	-2.13	2.12

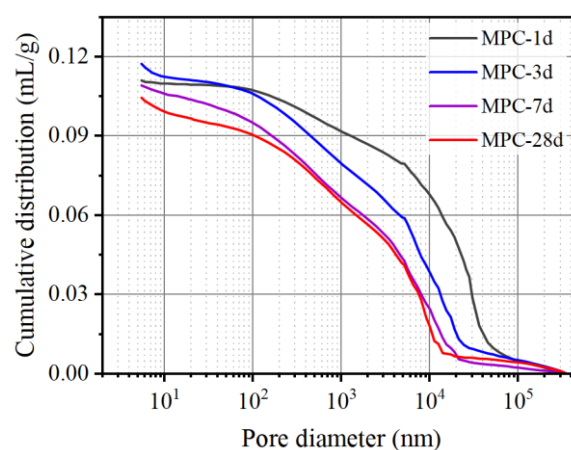
### 3.3 Microstructural characteristics

#### 3.3.1 Pore structure characteristics

The pore structure characteristics of MPC at different curing ages are shown in Fig. 8 and Table 7, respectively. The porosity values of MPC at 1, 3, 7 and 28 d are 22.27%, 23.48%, 22.01% and 21.26%, respectively. With increasing curing age, the porosity of MPC decreases slightly, while the overall change is minimal. However, the differential distribution curve shows that with the increase of curing age, the proportion of macropores gradually drops, while that of micropores gradually rises. From 1 d to 28 d, the most probable aperture of MPC decreases from 30.30 nm to 8.98 nm, and the average aperture goes down from 355.72 nm to 87.21 nm. Although the porosity of MPC has almost no change over 28 d, the pore structure is constantly refined with the increase of curing age, which can be ascribed to the formation of new hydration products or phase transformation, resulting in the gradual densification of microstructure.



(a)



(b)

Fig. 8. Pore size distribution of MPC at various curing ages: (a) differential distribution and (b) cumulative distribution.

Table 7 Pore structure characteristics of MPC at various curing ages.

Sample	Porosity (%)	Median pore diameter (nm)	Average pore diameter (nm)	Most probable aperture ( $\mu\text{m}$ )
MPC-1d	22.27	8.93	355.72	30.30
MPC-3d	23.48	7.10	114.69	13.76
MPC-7d	22.01	10.37	119.77	12.39
MPC-28d	21.26	8.08	87.21	8.98

### 3.3.2 Morphology

Typical BSEM images of MPC are displayed in Fig. 9(a) and (b), indicating that in the microstructure of MPC, there are mainly two types of areas: (1) columnar large-size grey–white areas, shown by red arrows, and (2) areas where dark grey particles and grey matter are mixed, indicated by blue arrows and yellow arrows. Among them, the columnar grey–white substance denotes the MKP crystal, the microscopic morphology of which is columnar or tabular [21, 48]. Many crystals are gathered to grow into a large columnar structure, and the columnar hydration products are connected into an MKP crystal cluster with a size of hundreds of microns, which is hereinafter referred to as a crystal region. Dark grey particles are unreacted magnesium oxide, as indicated by blue arrows. Light grey substances are the amorphous phases in hydration products, as indicated by yellow arrows. Unreacted magnesium oxide is distributed in amorphous hydration products and will be referred to as the hybrid region. Black substances are holes, as indicated by purple arrows. Some pores are distributed in hydration products as the volume of hydration products is smaller than that of the reactants during hydration process. If the hydration product is MKP crystal, the theoretical volume ratio of reactant to reaction product is 1.12. On one hand, the hydration products fill the original pores of MPC; on the other hand, there may be new pores in the middle of hydration products.

Using the hybrid region in Fig. 9(b) as an example, segmentation based on grey levels was carried out to identify the distribution of the different phases, as shown in Fig. 9(c). Black areas represent holes, while blue, yellow, red and green areas stand for magnesium oxide, amorphous phase reaction products, crystalline MKP and impurities, respectively. The distribution of the large MKP crystal clusters in the red area, as well as the mixing of blue (unreacted magnesium oxide) and yellow (amorphous phase hydration products) areas, can be clearly observed.

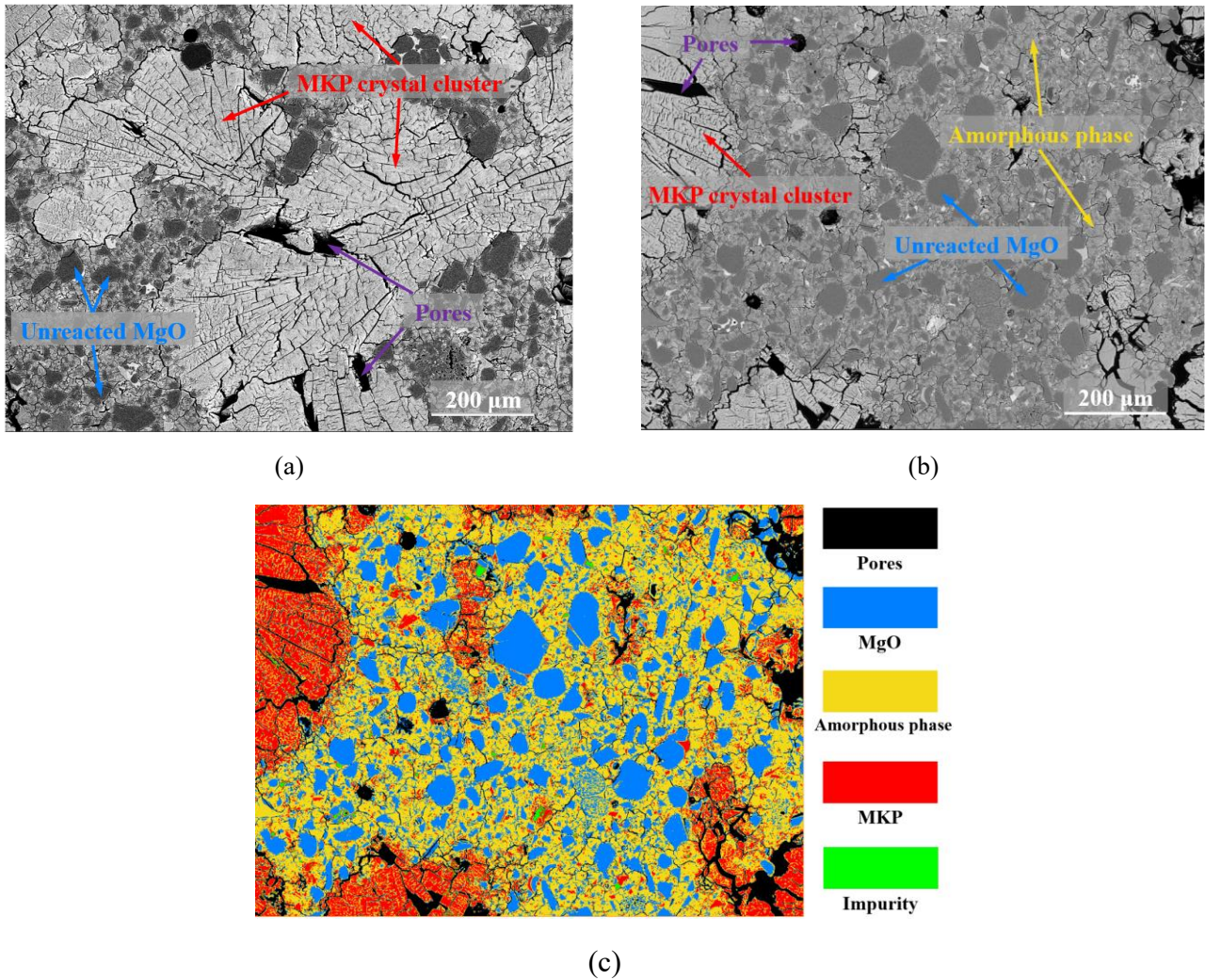
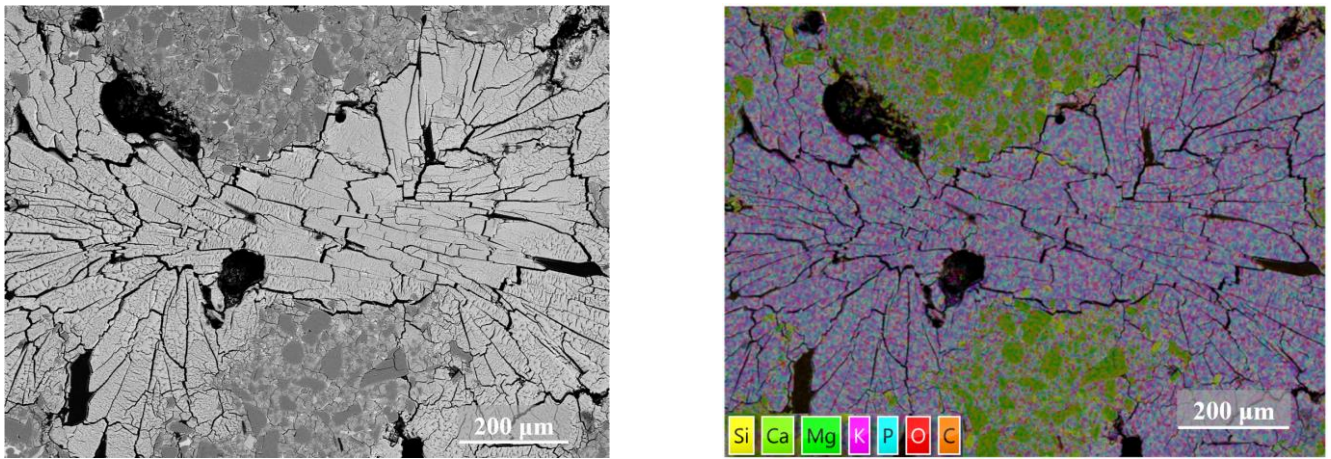


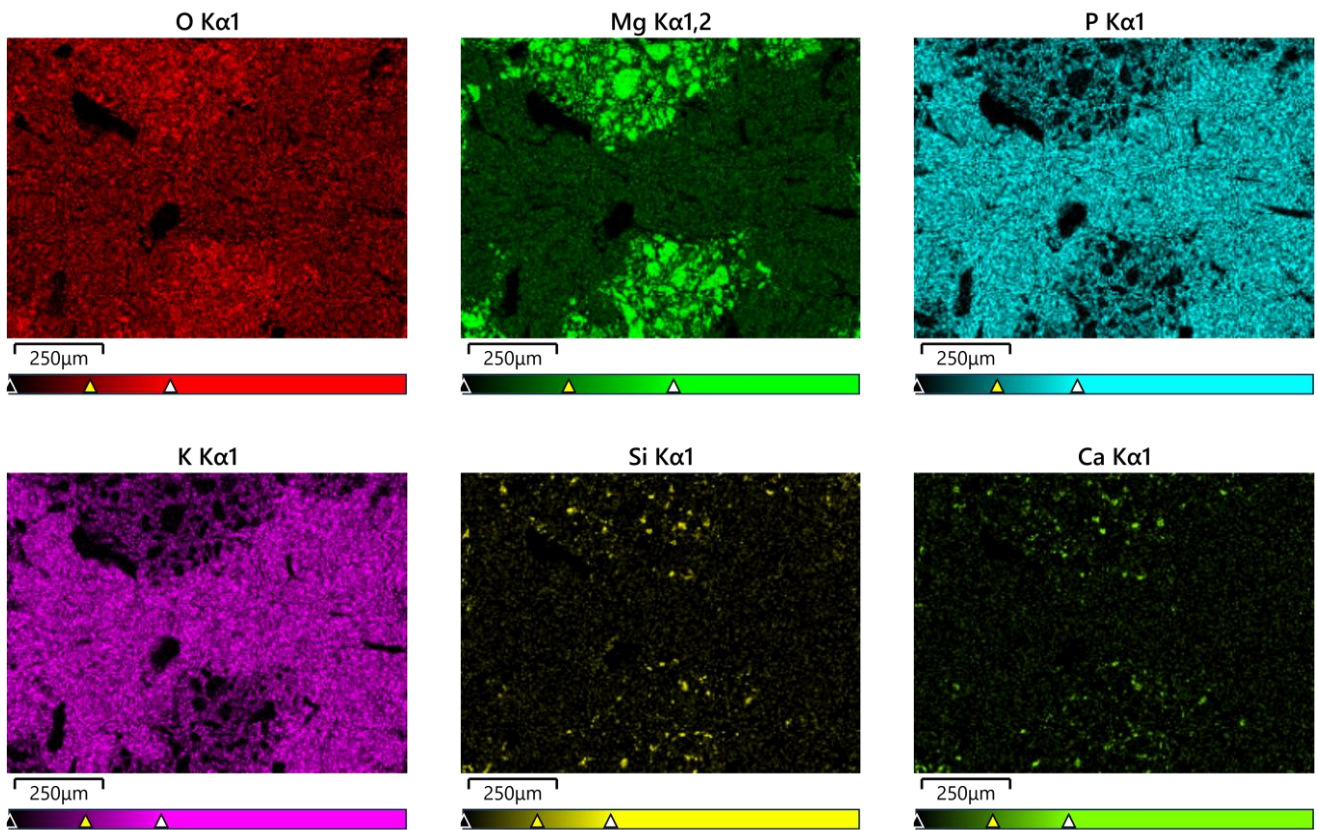
Fig. 9. Typical BSEM images of MPC: (a) crystal region and (b) hybrid region, and (c) distribution of different phases in hybrid region of MPC.

Figs. 10 and 11 show the typical EDS plane distributions of the MPC crystal region and the hybrid region. There are four elements, including O, Mg, P and K, distributed in the crystal region, which conform to the elemental composition of MKP. In the hybrid region, the highlighted areas of Mg and O are highly coincident, and there is no distribution of P and K in these areas, associated with the distribution area of magnesium oxide particles. The areas where the distribution of P and K is highly coincident are the areas where hydration products are distributed. In addition, in the hybrid region, small amounts of Si and Ca can be found, which are often distributed around magnesium oxide particles, may due to the impurity of  $\text{CaMgSiO}_4$  contained in the raw material of magnesium oxide.



(a)

(b)



(c)

Fig. 10. Typical EDS plane distribution in the crystal region of MPC: (a) BSEM image, (b) integrated element plane distribution, and (c) single element plane distribution.

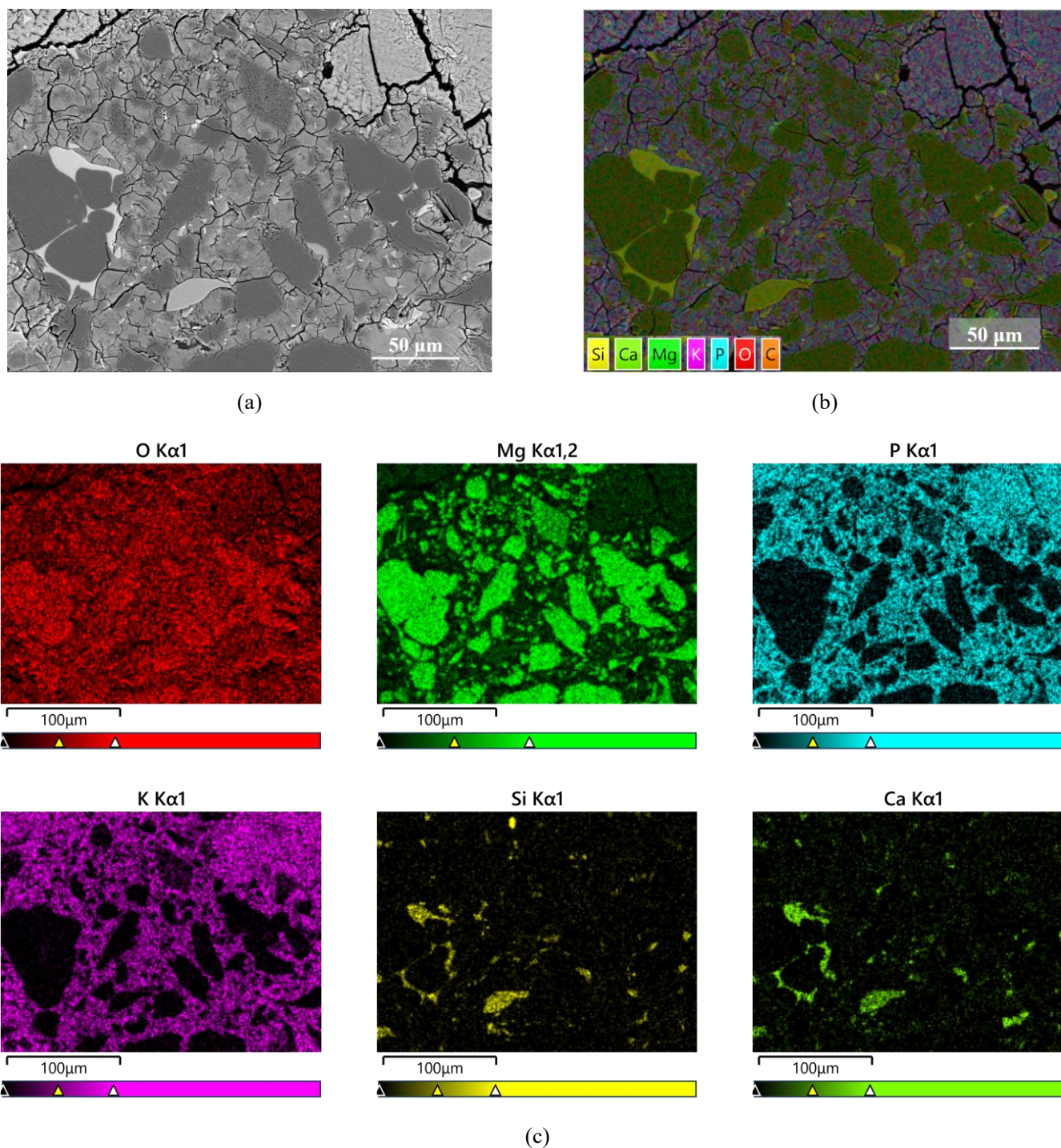


Fig. 11. Typical EDS plane distribution in the hybrid region of MPC: (a) BSEM image, (b) integrated element plane distribution, and (c) single element plane distribution.

At each curing age, the amorphous phase in the hybrid region is analysed by point EDS. The EDS distribution of points is demonstrated with the ratio of Mg/P and K/P as horizontal and vertical coordinates, respectively, as illustrated in Fig. 12. The theoretical ratio of K/P and Mg/P in  $\text{KMgPO}_4 \cdot \text{XH}_2\text{O}$  is 1, as indicated in the position of the red triangle in the figure. The coordinates of  $\text{MgHPO}_4$  and  $\text{Mg}_3(\text{PO}_4)_2$  in the element scale diagram are (1, 0) and (1.5, 0), respectively, as shown

with the green and orange triangle positions, respectively. At all curing ages, most EDS points are distributed around the coordinates (0.8, 0.75), and a few points have Mg/P ratios greater than 1. The ratios of K, Mg and P in the amorphous phase are close to 1, suggesting that the amorphous phase may contain a large amount of  $\text{KMgPO}_4 \cdot \text{XH}_2\text{O}$ .  $\text{Mg}_3(\text{PO}_4)_2$  may also be mixed in the amorphous phase, resulting in Mg/P ratios greater than 1 and K/P ratios less than 1 at some points. The specific phase composition of the amorphous phase needs further analysis using NMR.

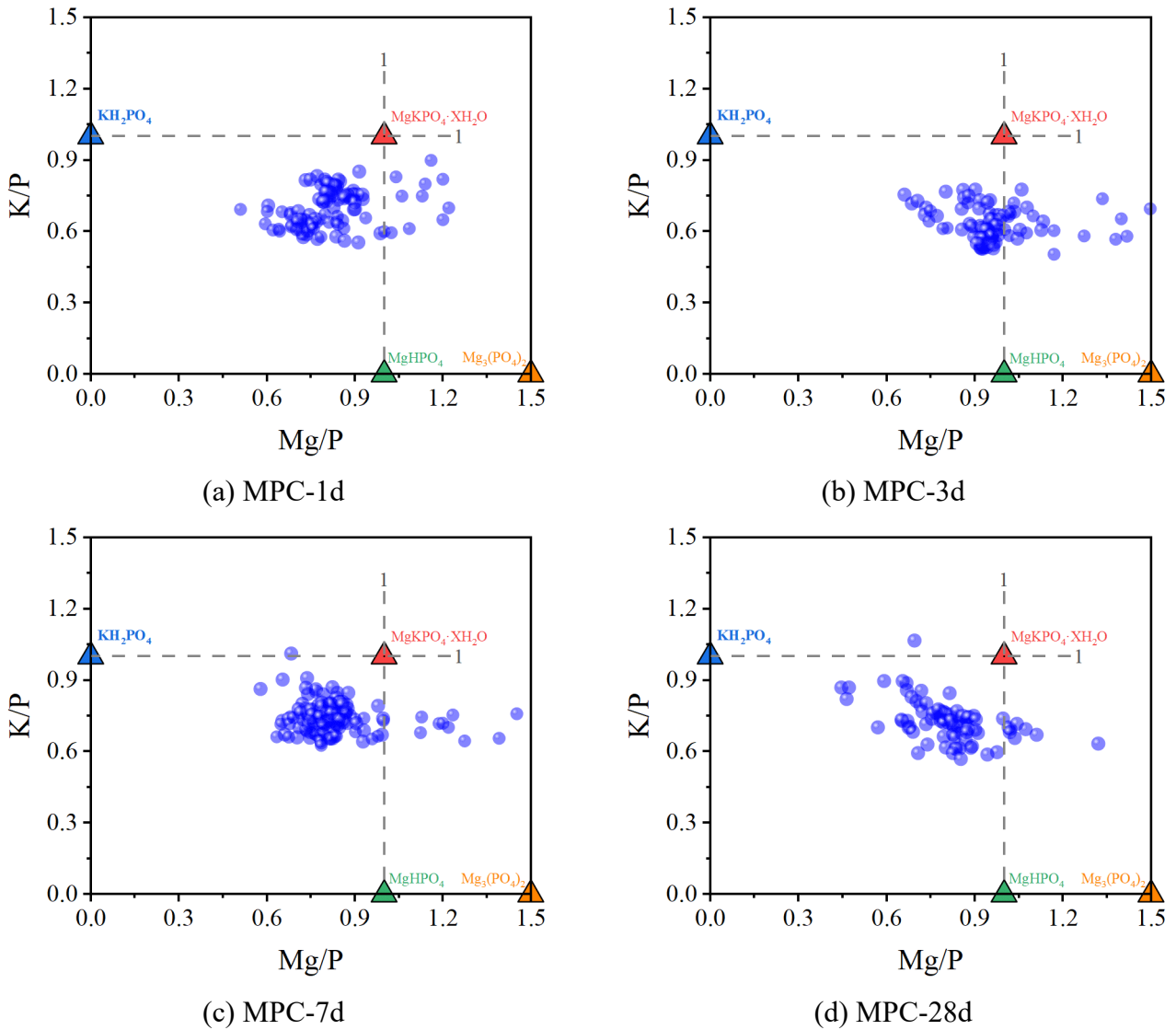


Fig. 12. EDS distribution of points in MPC at different curing ages.

### 3.4 Micromechanical properties

Grid and classic nanoindentation tests are used to study the relationship of the micromechanical properties of MPC with respect to curing age. Qualitative and quantitative analyses are carried out. Previous studies have successfully determined the composition and variation of hydration products of Portland cement with nanoindentation experiments [49, 50].

### 3.4.1 Analysis of typical phases

The micromechanical properties of typical phases (unreacted magnesium oxide and reaction products) in MPC are measured using nanoindentation conducted at 30 positions in the unreacted MgO and reaction product phases. Fig. 13 displays the corresponding indentation load–displacement curves. When the indentation load is 2 mN, the displacement range is very wide, meaning that the elastic modulus and hardness of different phases are significantly different. Among them, the displacement of the unreacted MgO curve in the deep red part is concentrated in the range of 67-98 nm, which is far smaller than that of the blue reaction product curve. This implies that the elastic modulus and hardness of unreacted MgO are relatively large. The displacement of the light red and blue curves of the reaction products is widely distributed in the range of 129-332 nm, suggesting that the components of hydration products are relatively complex and the micromechanical properties of them are quite different.

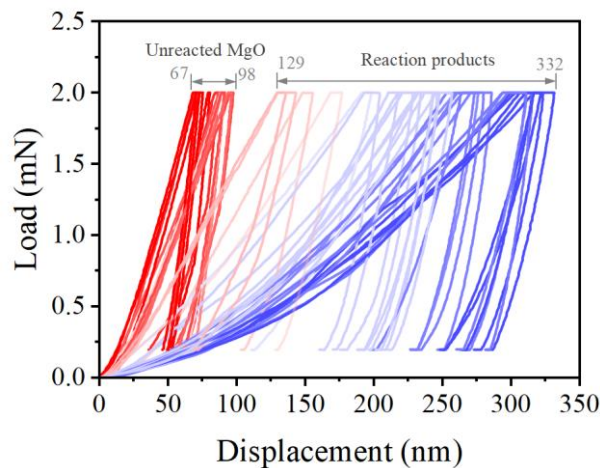


Fig. 13. Indentation load–displacement curves of the typical phases in MPC.

### 3.4.2 Phase analysis in the crystal region

According to the BSEM results, the microstructure of MPC can be divided into a crystal region and a hybrid region. At different curing ages, nanoindentation tests were conducted in the crystal region and hybrid region of MPC. Among them, a 4×4 matrix indentation test was carried out in the crystal region at each curing age. A scatter plot of the elastic modulus and hardness of indentation points in the crystal region was created (Fig. 14). The elastic modulus and hardness distribution in the crystal region are relatively concentrated at approximately 20 GPa and 1.25 GPa, respectively, and thus the micromechanical properties in the crystal region have strong stability. The mean and variance of the indentation results are further calculated, as given in Table 8 and Fig. 15. At different

curing ages, the mean value of the elastic modulus fluctuates slightly in the range of 19-22 GPa, with little difference, and the corresponding variance varies in the range of 1.0-1.6. Moreover, the average hardness is approximately 1.15 GPa, and the variance is approximately 0.1. The elastic modulus and hardness in the crystal region are highly consistent and have no evident change with curing age. Therefore, the indentation results reflect the micromechanical properties of the phase itself in the crystal region. The average values of elastic modulus and hardness of all indentation points in the crystal region are 20.18 GPa and 1.15 GPa, respectively.

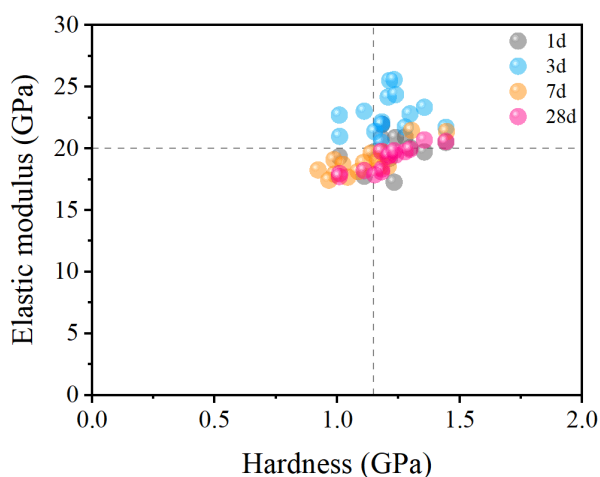
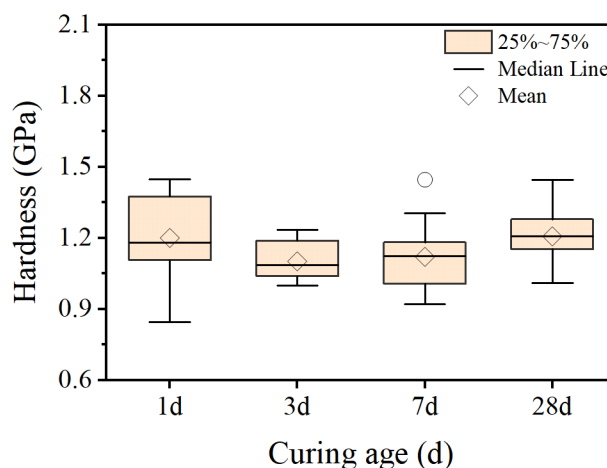
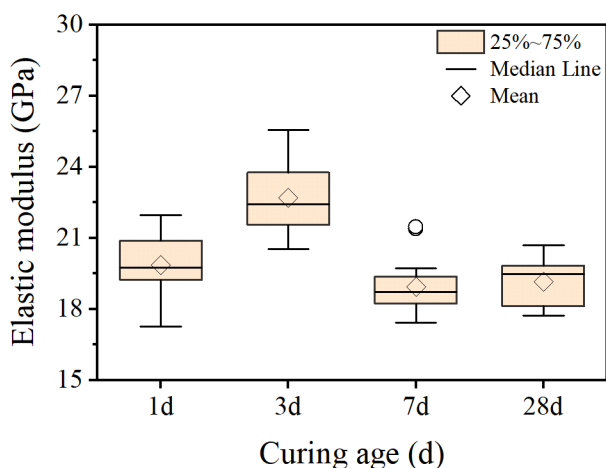


Fig. 14. Nanoindentation test results in the crystal region of MPC.

Table 8 Summary of nanoindentation results in the crystal region of MPC.

Sample	Elastic modulus (GPa)		Hardness (GPa)	
	Means	Variance	Means	Variance
MPC-1d	19.87	1.39	1.20	0.18
MPC-3d	22.63	1.55	1.10	0.08
MPC-7d	18.94	1.15	1.12	0.13
MPC-28d	19.14	1.00	1.21	0.12



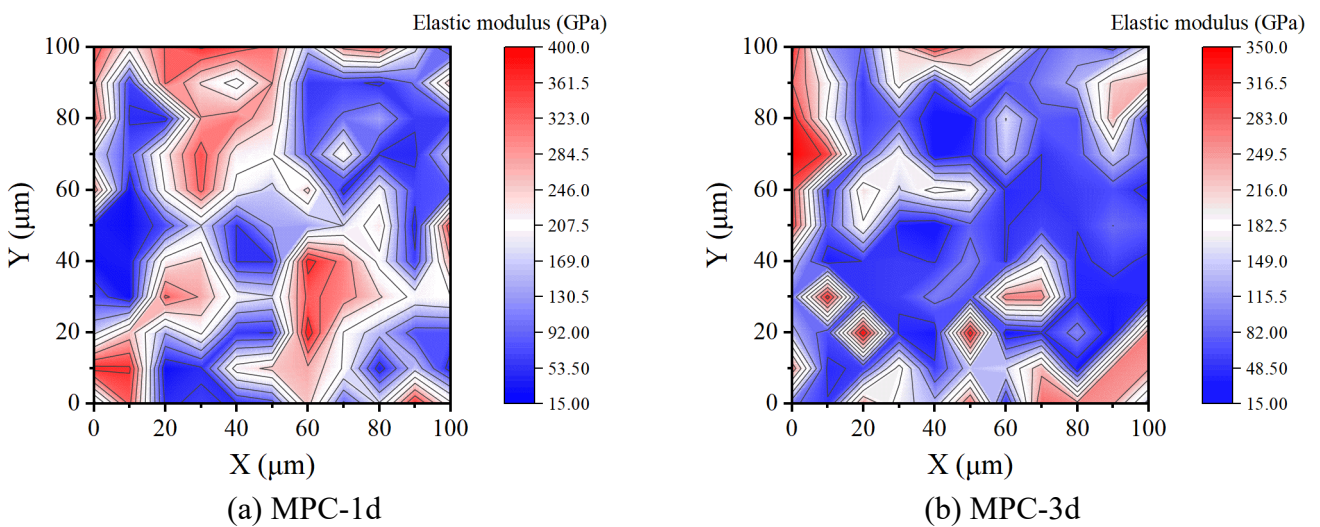
(a) (b)

Fig. 15. Elastic modulus and hardness box diagram in the crystal region of MPC.

### 3.4.3 Phase analysis in the hybrid region

#### 3.4.3.1 Qualitative analysis

At different curing ages,  $11 \times 11$  matrix points are selected in the MPC hybrid area for the grid nanoindentation test, and the matrix spacing is  $10 \mu\text{m}$ . The elastic modulus and hardness data of the indentation matrix test are plotted as contour maps, as shown in Fig. 16. The elastic modulus and hardness vary in the ranges of 14-400 GPa and 0-24 GPa, respectively. The elastic modulus and hardness of the red area are relatively large, while the elastic modulus and hardness of the blue area are relatively small. According to the microstructure distribution shown by BSEM (Fig. 9) and the indentation load–displacement curve of the typical phase (Fig. 13), the red area and the blue area correspond to the unreacted magnesium oxide and the reaction product, respectively. In the contour map of MPC-1d, the red area is widely distributed, meaning there is more magnesium oxide in the measured area. With increasing curing age, the red area gradually decreases, and the dark blue area gradually increases; the content of magnesium oxide decreases, while the content of reaction products increases. In addition, the distribution of the elastic modulus and hardness contour map is essentially consistent at all curing ages. The elastic modulus and hardness have a high positive correlation. Therefore, in the following sections, the elastic modulus is mainly selected for further quantitative analysis.



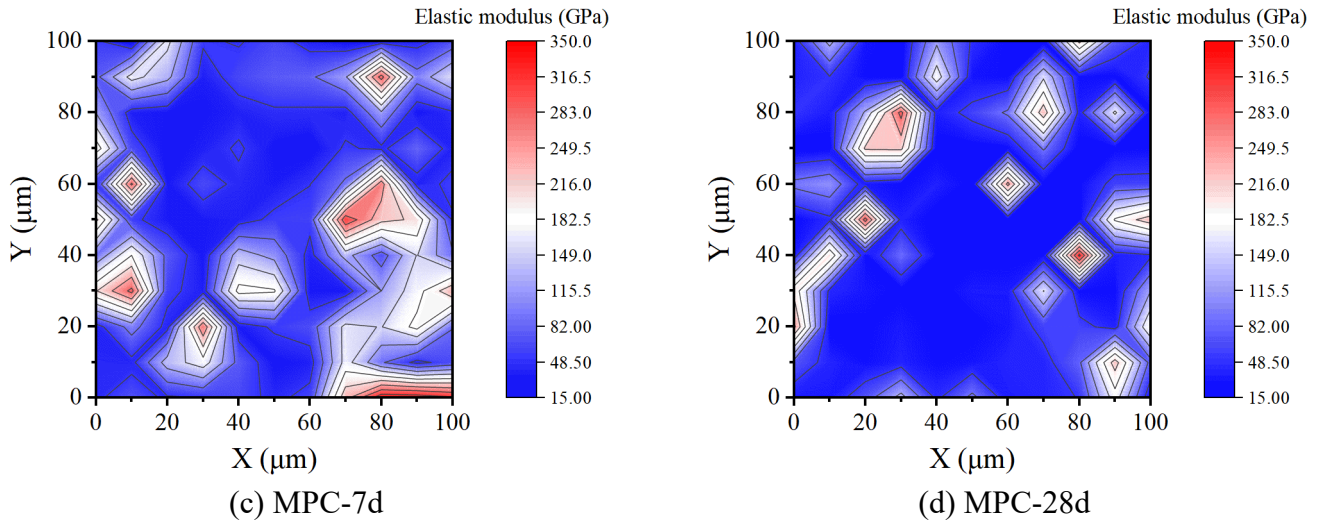


Fig. 16 Nanoindentation test results in hybrid regions.

### 3.4.3.2 Quantitative analysis

The micromechanical properties of hydration products in the hybrid region of MPC change greatly, and the components are complex. Thus, the statistical Gaussian deconvolution method was used to analyse the elastic modulus of different phases in MPC and evaluate the evolution of the elastic modulus with curing age. The MPC-1d sample is taken as an example to show the analysis process. Initially, a histogram of the elastic modulus data is created with a bin size of 20 GPa. Then, frequency density fitting of the elastic modulus is performed based on the histogram [51], as shown in Fig. 17(a). Assuming that the elastic modulus distribution of the phase conformed to a Gaussian distribution [52], deconvolution fitting was performed based on the experimental data to obtain three fitting distribution curves. The dotted line is the cumulative fitting curve, as shown in Fig. 17(b). The three curves correspond to the elastic modulus distribution of phase 1, phase 2 and phase 3, respectively, with mean values of 51.4 GPa, 186.3 GPa and 316.1 GPa, respectively. According to the XRD, BSEM and typical indentation test results, one of the phases is unreacted magnesium oxide. The elastic modulus of magnesium oxide was reported to be approximately 300 GPa [32, 33], which is close to the average value of phase 3. Therefore, the red Fit 3 curve is the elastic modulus distribution of magnesium oxide, as shown in Fig. 17(b). According to NMR analysis, phase 1 and phase 2 should be  $\text{MgKPO}_4$  and  $\text{Mg}_3(\text{PO}_4)_2$  in the amorphous phases.

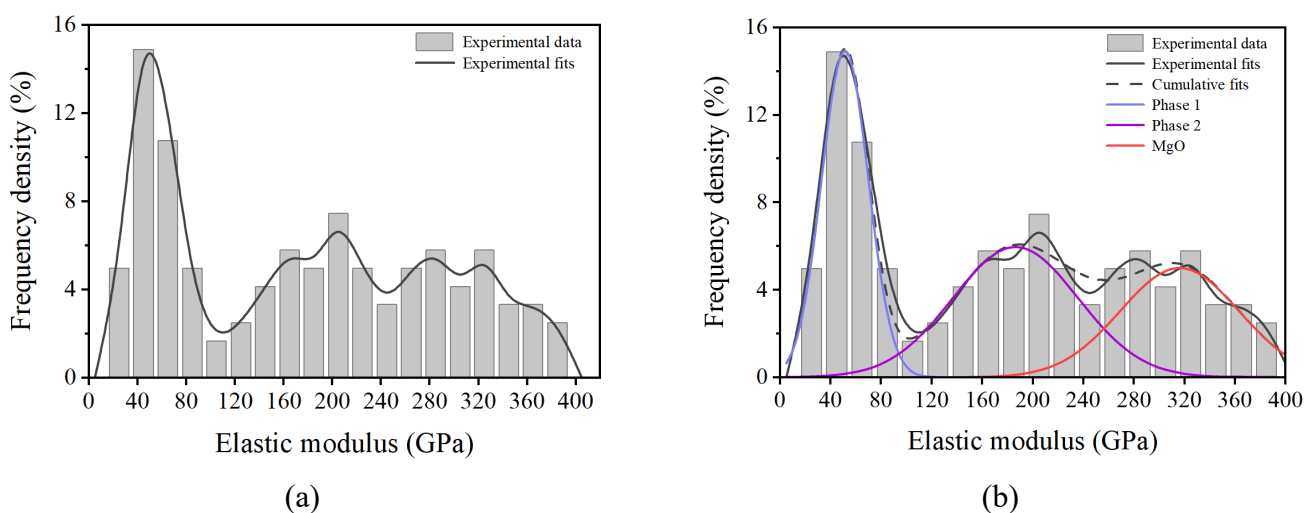


Fig. 17. Elastic modulus distribution of MPC-1d and deconvolution schematic diagram.

The deconvolution of the elastic modulus distribution, the scatter plot of the elastic modulus and hardness of MPC at different curing ages are presented in Fig. C. In the scatter diagram on the left, the blue, purple and red scatters correspond to phase 1, phase 2 and MgO, respectively. In the scatter plot, with increasing curing age, an increasing number of points tend to be located in the lower left corner, indicating that the elastic modulus and hardness tend to be smaller. Among them, the red scattered points of magnesium oxide decrease with curing age, and their distribution shifts to the left and down as a whole. Based on the average value and area ratio of the deconvolved Gaussian distribution curve in Fig. C, the elastic moduli and volume fractions of the phases at different curing ages are obtained, as shown in Fig. C. The elastic modulus of phase 1 decreases from 51.4 GPa to 29.2 GPa, while the volume fraction goes up from 34.3% to 72.7% with increasing curing age. This means that the content of phase 1 increases gradually with curing age, and the elastic modulus is closer to the elastic modulus of crystalline MKP, i.e., 20.2 GPa. The elastic modulus and volume fraction of phase 2 drop from 186.3 GPa and 37.1% to 142.3 GPa and 18.52%, respectively, with increasing curing age. The micromechanical properties of MgO reduce gradually with curing age. According to the analysis of  $^{31}\text{P}$  NMR spectra, the content of amorphous  $\text{MgKPO}_4$  gradually increases, while the content of amorphous  $\text{Mg}_3(\text{PO}_4)_2$  drops with increasing curing age. Therefore, phase 1 and phase 2 are amorphous  $\text{MgKPO}_4$  and amorphous  $\text{Mg}_3(\text{PO}_4)_2$ , respectively. The elastic modulus of amorphous  $\text{MgKPO}_4$  decreases gradually with time and approaches that of the MKP crystal. This suggests that the molecular structure of amorphous  $\text{MgKPO}_4$  changes and tends to transform into crystalline MKP. The grid nanoindentation test was carried out in the region of  $100 \times 100 \mu\text{m}$ , and thus the statistical results may not completely represent the phase content change in the whole MPC

sample but could be used to characterise the change trend of the micromechanical properties and distribution of the phase with time.

Table 9 Elastic modulus and volume fraction of each phase in the hybrid region of MPC.

Sample	Phase 1		Phase 2		MgO	
	E (GPa)	Volume (%)	E (GPa)	Volume (%)	E (GPa)	Volume (%)
MPC-1d	51.4	34.3	186.3	37.1	316.1	28.6
MPC-3d	49.0	48.5	172.2	26.7	297.1	20.3
MPC-7d	45.7	66.9	161.7	24.2	293.7	8.8
MPC-28d	29.2	72.7	142.3	18.52	273.6	8.7

### 3.5 Macroscopic mechanical properties

Fig. 18 displays the compressive and flexural strengths of MPC at different curing ages, which gradually increase with the increase of curing age. The compressive strength gradually goes up from 18.7 MPa at 1 d to 29.5 MPa at 7 d and then significantly rises to 53.0 MPa at 28 d. The flexural strength of MPC is 8.4 MPa at 1 d and then increases to 12.7 MPa at 28 d. The flexural strength increases slowly with curing age.

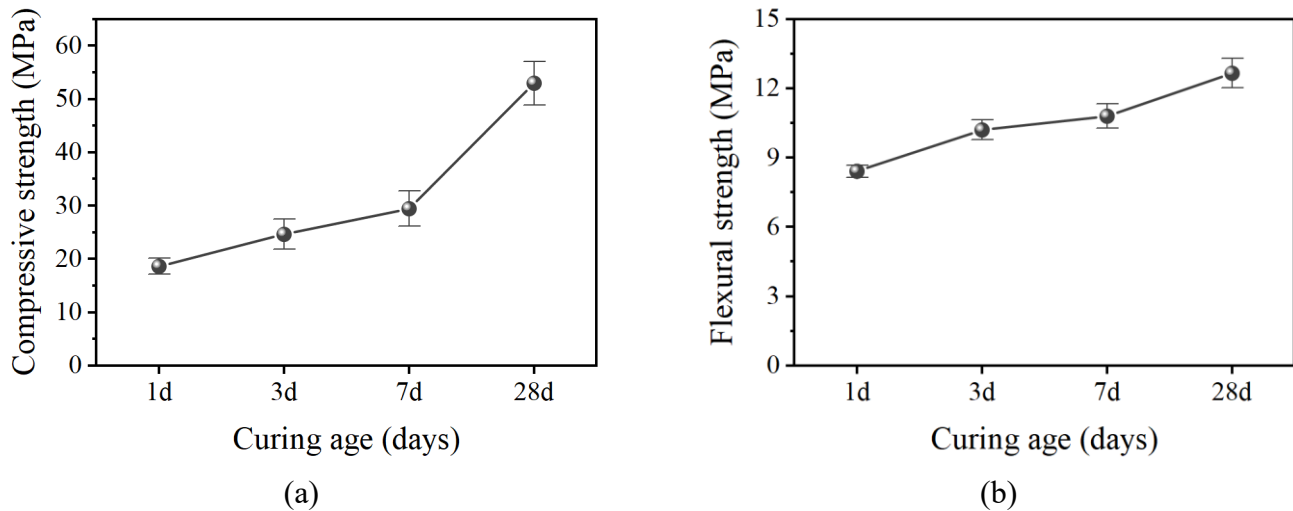


Fig. 18. Compressive and flexural properties of MPC at different curing ages: (a) compressive strength, and (b) flexural strength.

It is indicated that MPC has a typical heterogeneous microstructure, including pores, unreacted magnesium oxide particles, and crystalline and amorphous reaction products. The microstructure and mechanical properties are closely related, and thus the micromechanical properties can help us understand the contribution of different substances to the mechanical properties of MPC. Therefore, this section discusses the relationship between the microstructure and mechanical properties of MPC.

As per the nanoindentation test results, the elastic modulus of MKP is 19 GPa, and the elastic

moduli of amorphous  $\text{MgKPO}_4$  and amorphous  $\text{Mg}_3(\text{PO}_4)_2$  are approximately 29 GPa and 142 GPa at 28 d, respectively. The elastic modulus of the crystalline region is lower than that of the amorphous region, which does not seem to conform to conventional understanding. The modulus discrepancy can be ascribed to the different molecular structures of crystalline MKP and amorphous reaction products. Therefore, it is understandable that the latter has a higher elastic modulus. In addition, the elastic moduli of amorphous  $\text{MgKPO}_4$  and amorphous  $\text{Mg}_3(\text{PO}_4)_2$  drop slightly with increasing curing age as the molecular structure of amorphous phase also changes with time. In the molecular structure of crystal MKP, the  $\text{K}^+$  ion is loosely coordinated to four water molecules at the base and more tightly to a  $\text{PO}_4$  oxygen at the apex of a tetragonal pyramid. The packing of the  $\text{Mg}^{2+}$ ,  $\text{K}^+$  and  $\text{PO}_4^{3-}$  ions occurs in planes approximately parallel to the (101) and (011) planes [53]. The  $\text{MgKPO}_4$  skeleton is composed of  $\text{MgO}_4$  and  $\text{PO}_4$  tetrahedra [54]. The structure of  $\text{Mg}_3(\text{PO}_4)_2$  may be described in terms of somewhat distorted  $\text{MgO}_6$  octahedra,  $\text{MgO}_5$  polyhedra, and nearly regular  $\text{PO}_4$  tetrahedra. The groups are linked together by sharing corners and edges to give a three-dimensional framework [55]. As seen in the XRD results (Table 3), a part of the amorphous phase is transformed into crystalline MKP. The infrared results (Fig. 5) also show a slight change in the phosphate vibration band.

With the increase of curing age, the micromechanical properties of the parts of hydrated products of MPC decrease, while the macroscopic compressive and flexural strengths of MPC increase (Fig. 18). This is possibly because the pore structure has a decisive influence on the macroscopic strength of MPC. The pore size distribution in Fig. 8 is further counted according to different pore size ranges, as displayed in Fig. 19. With increasing curing age, the content of pores with sizes less than 10  $\mu\text{m}$  rises significantly, and the volume fraction of pores less than 0.1  $\mu\text{m}$  goes up from 4% at 1 d to 15% at 28 d. However, the volume of pores larger than 10  $\mu\text{m}$  visibly drops, and the content of pores in the range of 10-100  $\mu\text{m}$  reduces from 56% at 1 d to 13% at 28 d. The porosity of MPC changes slightly with time, but the pore structure changes remarkably. The pore size gradually refines, and the structure tends to be compact as new hydration products fill the original large pores and smaller pores form at the same time. Thus, the change in the macroscopic strength of MPC mainly depends on the compactness of pore structure rather than the micromechanical properties of hydration products. Such finding is in good agreement with those reported for Portland cement and alkali-activated cement systems that macroscopic mechanical properties are highly dependent on the pore structure of paste [49, 56].

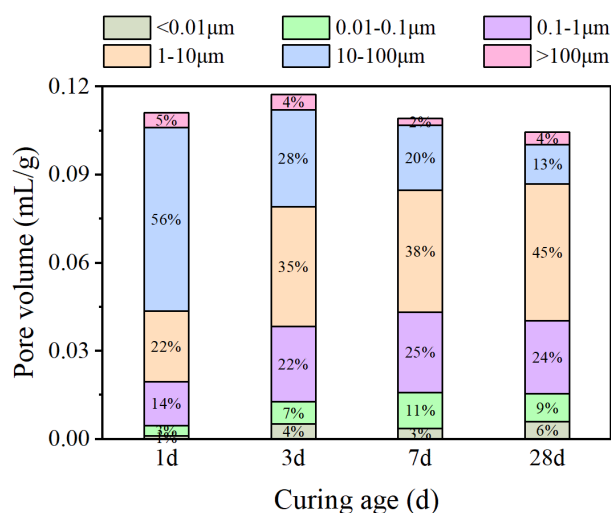


Fig. 19. Statistical diagram of pore size distribution of MPC.

#### 4. Conclusions

In this study, the microstructure and micromechanical properties of MPC were investigated through a series of experimental tests. Based on the obtained results, the main conclusions can be drawn as follows:

(1) MPC was mainly composed of MgO, MKP crystal and amorphous hydration products. It was indicated in the  $^{31}\text{P}$  and  $^1\text{H}$ - $^{31}\text{P}$  NMR analysis that the amorphous hydration products were most likely  $\text{MgKPO}_4$  and  $\text{Mg}_3(\text{PO}_4)_2$ .

(2) With the increase of curing age, the porosity of MPC decreased minimally, while the pore structure changed significantly. The microstructure of MPC mainly consisted of two types of regions: a crystal region with columnar MKP crystal clusters up to hundreds of microns in size and a hybrid region where unreacted magnesium oxide and amorphous hydrates were mixed.

(3) The elastic modulus and hardness of MKP crystal and amorphous hydration products were characterised using nanoindentation, indicating that the macroscopic strength of MPC mainly depended on the compactness of pore structure rather than the micromechanical properties of hydration products.

#### Acknowledgements

The authors gratefully acknowledge the financial support from the National Key Research and Development Plan Project (No. 2022YFC3803103) and the National Natural Science Foundation of China (No. 52078015).

#### References

[1] S.A. Walling, J.L. Provis, Magnesia-based cements: a journey of 150 years, and cements for the

future?, *Chemical reviews*, 116 (2016) 4170-4204.

[2] H. Jiang, J. Zhang, T. Li, Y. Wang, Y. Liu, H. De Backer, Feasibility analysis of magnesium phosphate cement as a repair material for base slab of China railway track system II ballastless track, *Construction and Building Materials*, 326 (2022) 126821.

[3] F. Liu, B. Pan, C. Zhou, Experimental Study on a Novel Modified Magnesium Phosphate Cement Mortar Used for Rapid Repair of Portland Cement Concrete Pavement in Seasonally Frozen Areas, *Journal of Materials in Civil Engineering*, 34 (2022) 04021483.

[4] X. Cao, Q. Zhang, W. Yang, L. Fang, S. Liu, R. Ma, K. Guo, N. Ma, Lead-chlorine synergistic immobilization mechanism in municipal solid waste incineration fly ash (MSWIFA)-based magnesium potassium phosphate cement, *Journal of Hazardous Materials*, 442 (2023) 130038.

[5] Y. Zhang, Z. Wan, L. Wang, B. Guo, B. Ma, L. Chen, D.C. Tsang, Designing magnesium phosphate cement for stabilization/solidification of zn-rich electroplating sludge, *Environmental Science & Technology*, 56 (2022) 9398-9407.

[6] X. Gu, Y. Li, C. Qi, K. Cai, Biodegradable magnesium phosphates in biomedical applications, *Journal of Materials Chemistry B*, (2022).

[7] W. Liu, Z. Huan, C. Wu, Z. Zhou, J. Chang, High-strength calcium silicate-incorporated magnesium phosphate bone cement with osteogenic potential for orthopedic application, *Composites Part B: Engineering*, 247 (2022) 110324.

[8] H. Lahalle, C.C.D. Coumes, A. Mesbah, D. Lambertin, C. Cannes, S. Delpech, S. Gauffinet, Investigation of magnesium phosphate cement hydration in diluted suspension and its retardation by boric acid, *Cement and Concrete Research*, 87 (2016) 77-86.

[9] M. Le Rouzic, T. Chaussadent, G. Platret, L. Stefan, Mechanisms of k-struvite formation in magnesium phosphate cements, *Cement and Concrete Research*, 91 (2017) 117-122.

[10] A. Viani, M. Pérez-Estébanez, S. Pollastri, A.F. Gualtieri, In situ synchrotron powder diffraction study of the setting reaction kinetics of magnesium-potassium phosphate cements, *Cement and Concrete Research*, 79 (2016) 344-352.

[11] T. Zhang, H. Chen, X. Li, Z. Zhu, Hydration behavior of magnesium potassium phosphate cement and stability analysis of its hydration products through thermodynamic modeling, *Cement and Concrete Research*, 98 (2017) 101-110.

[12] M.A. Haque, B. Chen, Research progresses on magnesium phosphate cement: A review,

Construction and building materials, 211 (2019) 885-898.

[13] B. Xu, F. Winnefeld, J. Kaufmann, B. Lothenbach, Influence of magnesium-to-phosphate ratio and water-to-cement ratio on hydration and properties of magnesium potassium phosphate cements, *Cement and Concrete Research*, 123 (2019) 105781.

[14] J. Qin, J. Qian, X. Dai, C. You, H. Ma, Z. Li, Effect of water content on microstructure and properties of magnesium potassium phosphate cement pastes with different magnesia - to - phosphate ratios, *Journal of the American Ceramic Society*, 104 (2021) 2799-2819.

[15] J. Shi, J. Zhao, H. Chen, P. Hou, S. Kawashima, J. Qin, X. Zhou, J. Qian, X. Cheng, Sulfuric acid-resistance performances of magnesium phosphate cements: Macro-properties, mineralogy and microstructure evolutions, *Cement and Concrete Research*, 157 (2022) 106830.

[16] B. Xu, F. Winnefeld, B. Ma, D. Rentsch, B. Lothenbach, Influence of aluminum sulfate on properties and hydration of magnesium potassium phosphate cements, *Cement and Concrete Research*, 156 (2022) 106788.

[17] A. Viani, G. Mali, P. Mácová, Investigation of amorphous and crystalline phosphates in magnesium phosphate ceramics with solid-state  $^1\text{H}$  and  $^{31}\text{P}$  NMR spectroscopy, *Ceramics International*, 43 (2017) 6571-6579.

[18] K. Sotiriadis, P. Mácová, A.S. Mazur, P.M. Tolstoy, A. Viani, A solid state NMR and in-situ infrared spectroscopy study on the setting reaction of magnesium sodium phosphate cement, *Journal of Non-Crystalline Solids*, 498 (2018) 49-59.

[19] A. Viani, P. Mácová, Polyamorphism and frustrated crystallization in the acid-base reaction of magnesium potassium phosphate cements, *CrystEngComm*, 20 (2018) 4600-4613.

[20] A. Viani, P. Mácová, K. Sotiriadis, Amorphous-crystalline transformation control on the microstructural evolution of magnesium phosphate cements, *Materials Letters*, 292 (2021) 129630.

[21] C. Chau, F. Qiao, Z. Li, Microstructure of magnesium potassium phosphate cement, *Construction and Building Materials*, 25 (2011) 2911-2917.

[22] B. Xu, H. Ma, Z. Li, Influence of magnesia-to-phosphate molar ratio on microstructures, mechanical properties and thermal conductivity of magnesium potassium phosphate cement paste with large water-to-solid ratio, *Cement and Concrete Research*, 68 (2015) 1-9.

[23] K. Velez, S. Maximilien, D. Damidot, G. Fantozzi, F. Sorrentino, Determination by nanoindentation of elastic modulus and hardness of pure constituents of Portland cement clinker,

Cement and Concrete Research, 31 (2001) 555-561.

[24] G. Constantinides, F.-J. Ulm, The effect of two types of CSH on the elasticity of cement-based materials: Results from nanoindentation and micromechanical modeling, *Cement and concrete research*, 34 (2004) 67-80.

[25] G. Constantinides, F.-J. Ulm, The nanogranular nature of C–S–H, *Journal of the Mechanics and Physics of Solids*, 55 (2007) 64-90.

[26] M. Vandamme, F.-J. Ulm, P. Fonollosa, Nanogranular packing of C–S–H at substoichiometric conditions, *Cement and Concrete Research*, 40 (2010) 14-26.

[27] D. Davydov, M. Jirasek, L. Kopecký, Critical aspects of nano-indentation technique in application to hardened cement paste, *Cement and Concrete Research*, 41 (2011) 20-29.

[28] K.J. Krakowiak, W. Wilson, S. James, S. Musso, F.-J. Ulm, Inference of the phase-to-mechanical property link via coupled X-ray spectrometry and indentation analysis: Application to cement-based materials, *Cement and Concrete Research*, 67 (2015) 271-285.

[29] W. Wilson, L. Sorelli, A. Tagnit-Hamou, Automated coupling of NanoIndentation and Quantitative Energy-Dispersive Spectroscopy (NI-QEDS): A comprehensive method to disclose the micro-chemo-mechanical properties of cement pastes, *Cement and Concrete Research*, 103 (2018) 49-65.

[30] C. Hu, Y. Ruan, S. Yao, F. Wang, Y. He, Y. Gao, Insight into the evolution of the elastic properties of calcium-silicate-hydrate (CSH) gel, *Cement and Concrete Composites*, 104 (2019) 103342.

[31] Y. Li, G. Zhang, Z. Wang, Z. Guan, Experimental-computational approach to investigate compressive strength of magnesium phosphate cement with nanoindentation and finite element analysis, *Construction and Building Materials*, 190 (2018) 414-426.

[32] J. Qin, H. Zhu, Z. He, X. Yu, J. Shi, J. Lu, C. Ma, Y. Cheng, Recycling of water treatment sludge into magnesium potassium phosphate cement component by a combination of silica fume, *Journal of Building Engineering*, 51 (2022) 104308.

[33] Z.-h. He, H.-n. Zhu, J.-y. Shi, J. Li, Q. Yuan, C. Ma, Multi-scale characteristics of magnesium potassium phosphate cement modified by metakaolin, *Ceramics International*, 48 (2022) 12467-12475.

[34] M. Morales, J. Formosa, E. Xuriguera, M. Niubo, M. Segarra, J. Chimenos, Elastic modulus of a chemically bonded phosphate ceramic formulated with low-grade magnesium oxide determined by

Nanoindentation, *Ceramics International*, 41 (2015) 12137-12146.

[35] M.A. Haque, B. Chen, Y. Maierdan, Influence of supplementary materials on the early age hydration reactions and microstructural progress of magnesium phosphate cement matrices, *Journal of Cleaner Production*, 333 (2022) 130086.

[36] Z. Zhang, Q. Wang, Z. Huang, Value-added utilization of copper slag to enhance the performance of magnesium potassium phosphate cement, *Resources, Conservation and Recycling*, 180 (2022) 106212.

[37] H. Ma, B. Xu, J. Liu, H. Pei, Z. Li, Effects of water content, magnesia-to-phosphate molar ratio and age on pore structure, strength and permeability of magnesium potassium phosphate cement paste, *Materials & Design*, 64 (2014) 497-502.

[38] Y. Li, W. Bai, T. Shi, A study of the bonding performance of magnesium phosphate cement on mortar and concrete, *Construction and Building Materials*, 142 (2017) 459-468.

[39] Y. Li, H. Lin, S.A.S. Hejazi, C. Zhao, M. Xie, The effect of low temperature phase change material of hydrated salt on the performance of magnesium phosphate cement, *Construction and Building Materials*, 149 (2017) 272-278.

[40] C. Chauhan, P. Vyas, M. Joshi, Growth and characterization of Struvite - K crystals, *Crystal Research and Technology*, 46 (2011) 187-194.

[41] P. Mácová, A. Viani, Investigation of setting reaction in magnesium potassium phosphate ceramics with time resolved infrared spectroscopy, *Materials Letters*, 205 (2017) 62-66.

[42] I. Mudrakovskii, V. Shmachkova, N. Kotsarenko, V. Mastikhin,  $^{31}\text{P}$  nmr study of I–IV group polycrystalline phosphates, *Journal of Physics and Chemistry of Solids*, 47 (1986) 335-339.

[43] H. Lahalle, C.C.D. Coumes, C. Mercier, D. Lambertin, C. Cannes, S. Delpech, S. Gauffinet, Influence of the w/c ratio on the hydration process of a magnesium phosphate cement and on its retardation by boric acid, *Cement and Concrete Research*, 109 (2018) 159-174.

[44] L.J. Gardner, S.A. Bernal, S.A. Walling, C.L. Corkhill, J.L. Provis, N.C. Hyatt, Characterisation of magnesium potassium phosphate cements blended with fly ash and ground granulated blast furnace slag, *Cement and Concrete Research*, 74 (2015) 78-87.

[45] L.J. Gardner, S.A. Walling, S.M. Lawson, S. Sun, S.A. Bernal, C.L. Corkhill, J.L. Provis, D.C. Apperley, D. Iuga, J.V. Hanna, Characterization of and structural insight into struvite-K,  $\text{MgKPO}_4 \cdot 6\text{H}_2\text{O}$ , an analogue of struvite, *Inorganic Chemistry*, 60 (2020) 195-205.

- [46] D. Hahn, A. Masoudi Alavi, V. Hopp, P. Quirnbach, Phase development of phosphate - bonded  $\text{Al}_2\text{O}_3$  -  $\text{MgAl}_2\text{O}_4$  high - temperature ceramics: XRD and solid - state NMR investigations, *Journal of the American Ceramic Society*, 104 (2021) 6625-6642.
- [47] S.N. Scrimgeour, J.A. Chudek, C.H. Lloyd, The determination of phosphorus containing compounds in dental casting investment products by  $^{31}\text{P}$  solid-state MAS-NMR spectroscopy, *Dental Materials*, 23 (2007) 415-424.
- [48] D. Wang, J. Zhu, R. Wang, Assessment of magnesium potassium phosphate cement for waste sludge solidification: Macro-and micro-analysis, *Journal of Cleaner Production*, 294 (2021) 126365.
- [49] G. Fang, M. Zhang, Multiscale micromechanical analysis of alkali-activated fly ash-slag paste, *Cement and Concrete Research*, 135 (2020) 106141.
- [50] R. Hay, J. Li, K. Celik, Phase evolution, micromechanical properties, and morphology of calcium (alumino) silicate hydrates C-(A-) SH under carbonation, *Cement and Concrete Research*, 152 (2022) 106683.
- [51] R. Thomas, B.S. Gebregziabiher, A. Giffin, S. Peethamparan, Micromechanical properties of alkali-activated slag cement binders, *Cement and Concrete Composites*, 90 (2018) 241-256.
- [52] Z. Luo, W. Li, Y. Gan, K. Mendu, S.P. Shah, Applying grid nanoindentation and maximum likelihood estimation for NASH gel in geopolymer paste: Investigation and discussion, *Cement and Concrete Research*, 135 (2020) 106112.
- [53] M. Mathew, L. Schroeder, Crystal structure of a struvite analogue,  $\text{MgKPO}_4 \cdot 6\text{H}_2\text{O}$ , *Acta Crystallographica Section B: Structural Crystallography and Crystal Chemistry*, 35 (1979) 11-13.
- [54] G. Wallez, C. Colbeau-Justin, T. Le Mercier, M. Quarton, F. Robert, Crystal chemistry and polymorphism of potassium–magnesium monophosphate, *Journal of Solid State Chemistry*, 136 (1998) 175-180.
- [55] A.G. Nord, P. Kierkegaard, The crystal structure of  $\text{Mg}_3(\text{PO}_4)_2$ , *Acta Chemica Scandinavica*, 22 (1968) 1466-1474.
- [56] J. Tatar, C.R. Taylor, H. Hamilton, A multiscale micromechanical model of adhesive interphase between cement paste and epoxy supported by nanomechanical evidence, *Composites Part B: Engineering*, 172 (2019) 679-689.

Appendix

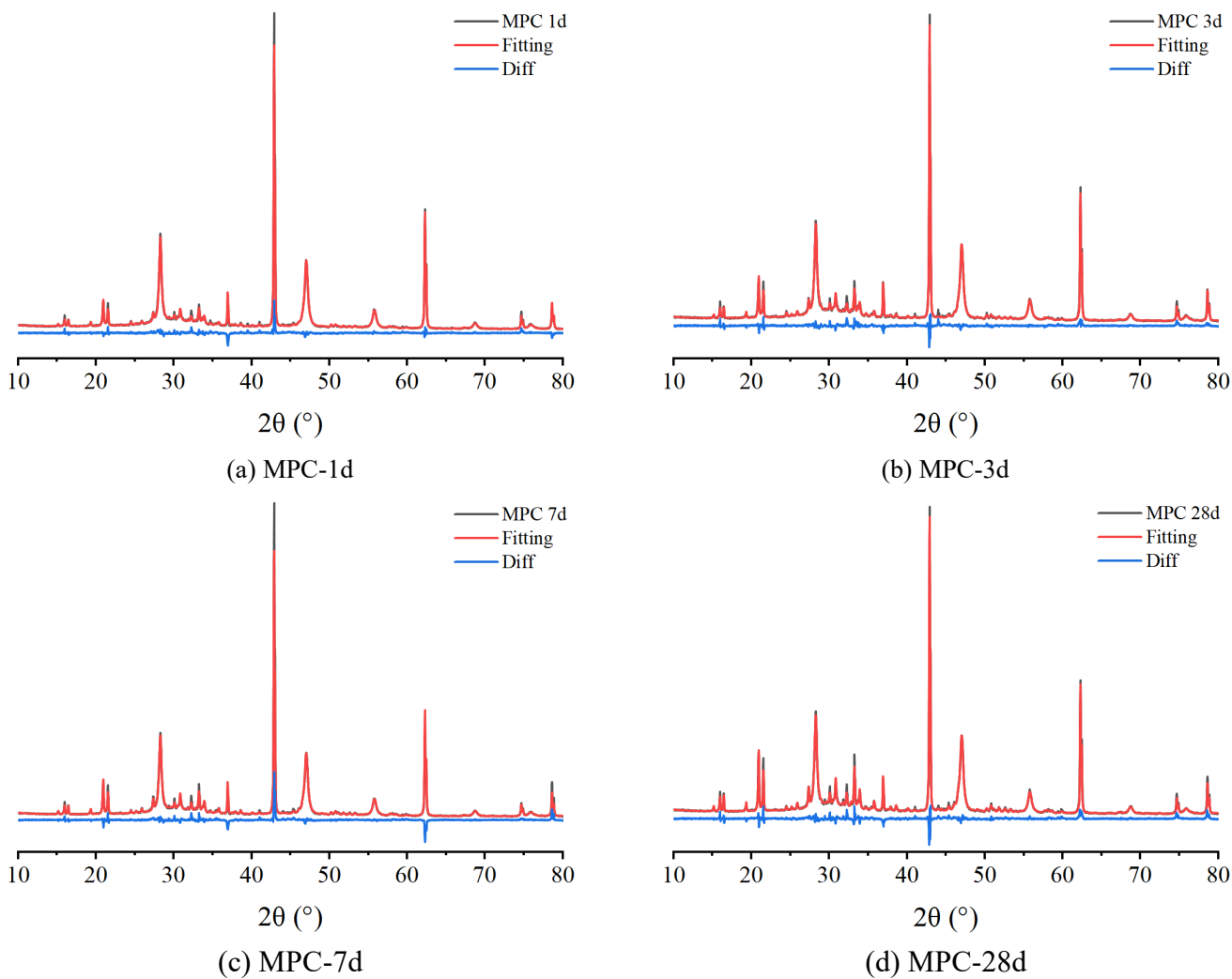
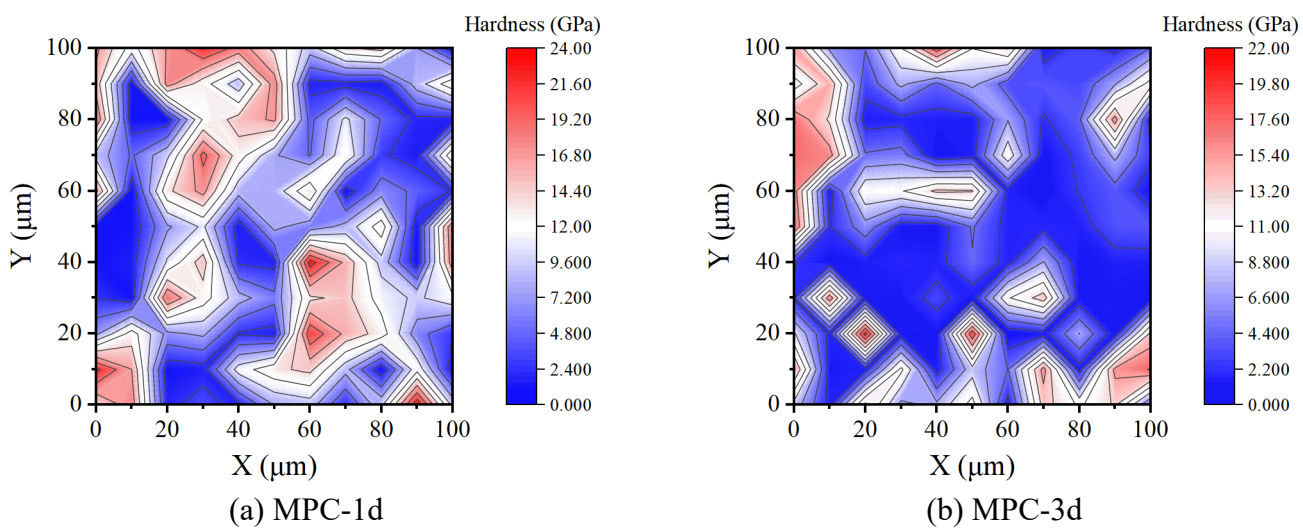
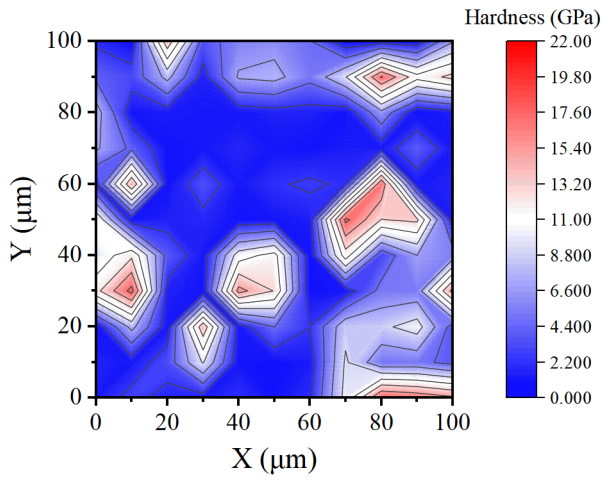
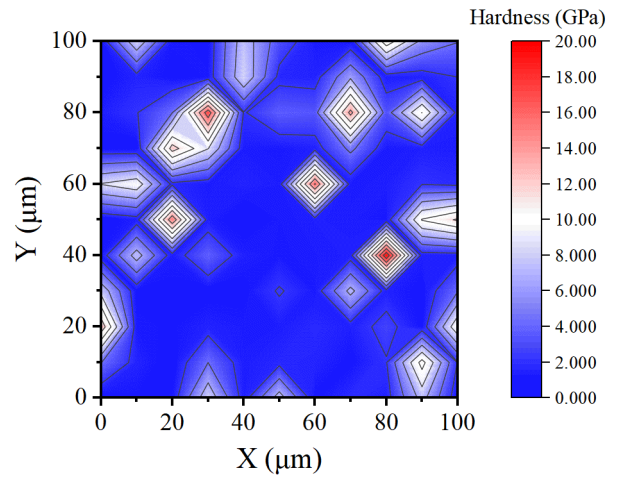


Fig. A. Fitting analysis of XRD curve of MPC.



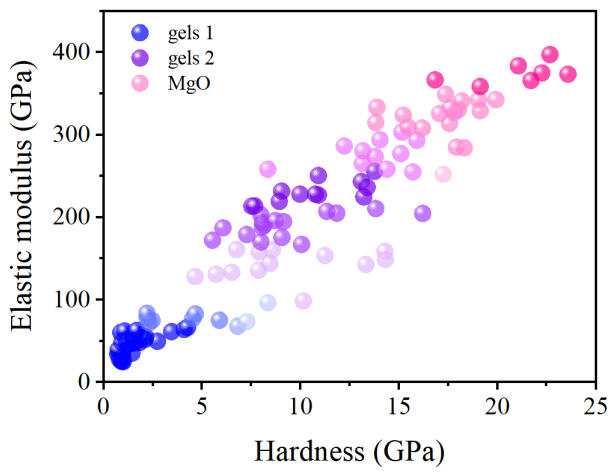


(c) MPC-7d

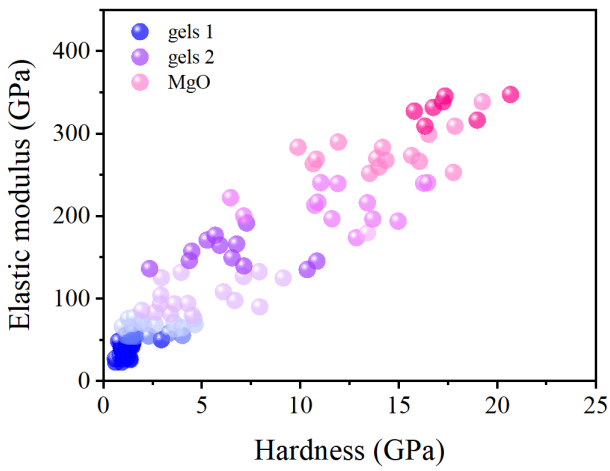
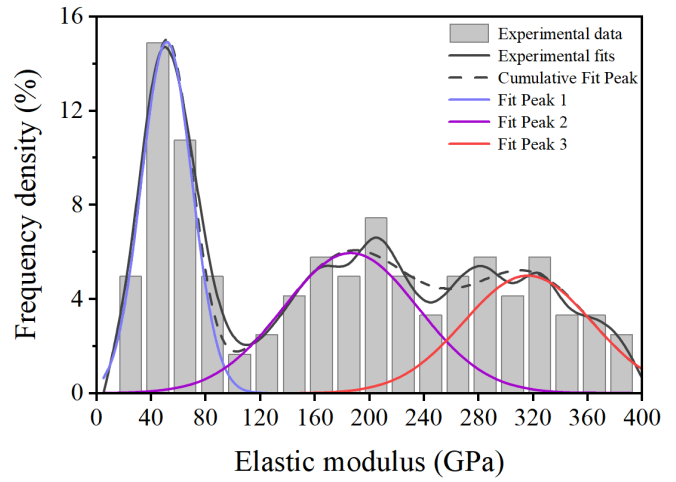


(d) MPC-28d

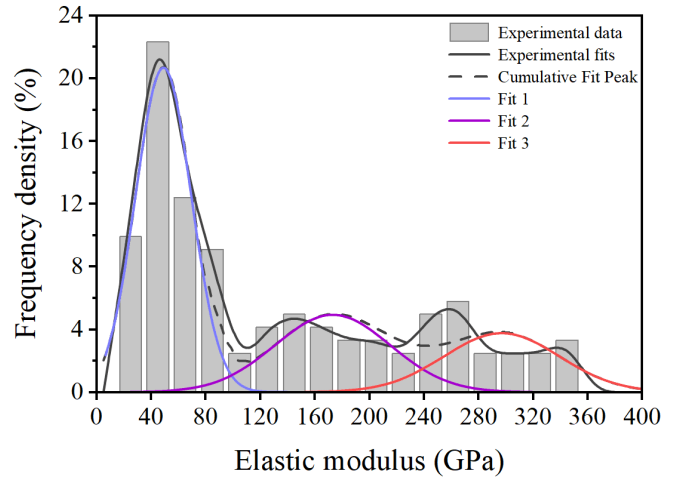
Fig. B. Nanoindentation test results in hybrid regions.

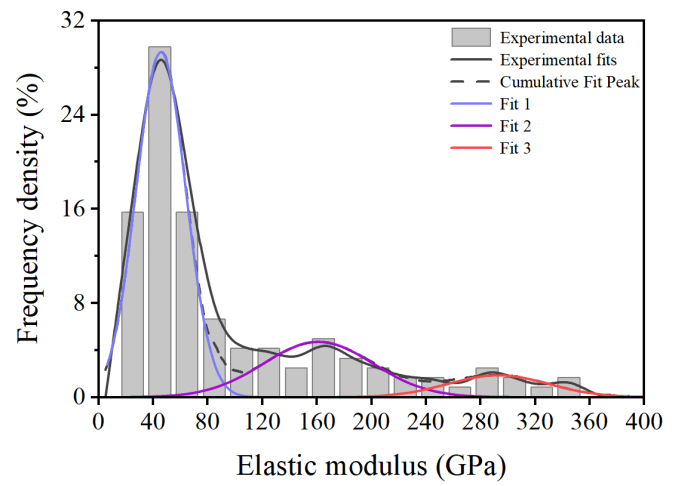
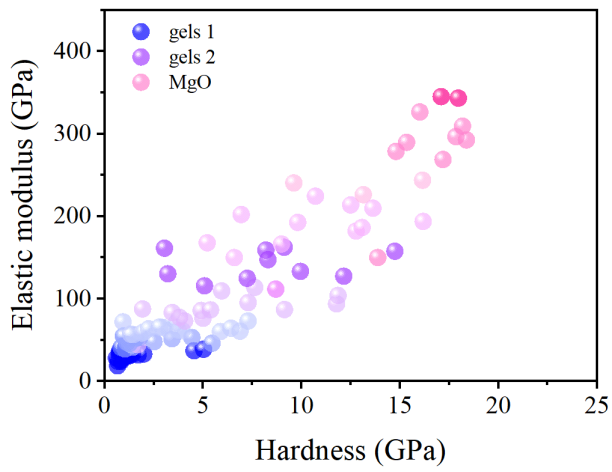


(a) MPC-1d

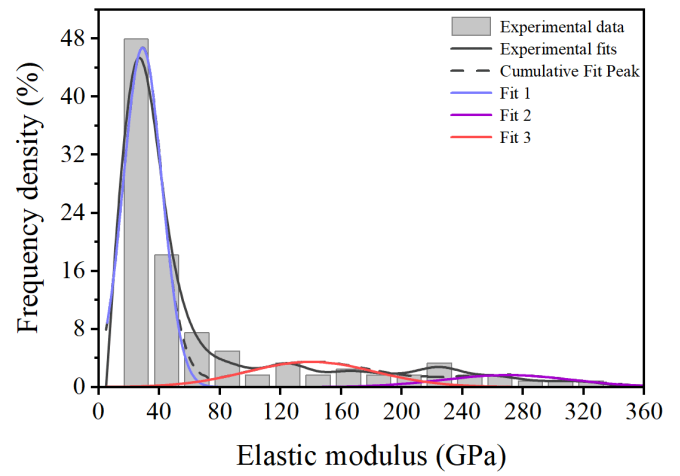
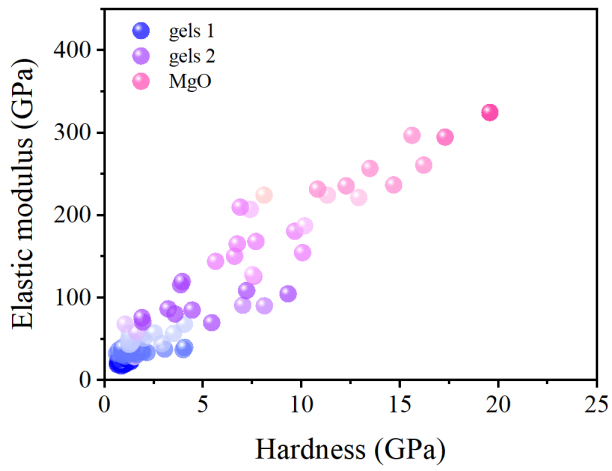


(b) MPC-3d





(c) MPC-7d



(d) MPC-28d

Fig. C. Scatter plot of elastic modulus versus hardness and deconvolution of elastic modulus distribution of MPC.